
Article:
Liu, Q orcid.org/0000-0002-1132-9392, Barker, R, Wang, C et al. (3 more authors) (2022) The corrosion behaviour of stainless steels and Ni-based alloys in nitrate salts under thermal cycling conditions in concentrated solar power plants. Solar Energy, 232. pp. 169-185. ISSN 0038-092X

https://doi.org/10.1016/j.solener.2021.12.072

The corrosion behaviour of stainless steels and Ni-based alloys in nitrate salts under thermal cycling conditions in Concentrated Solar Power plants

Qingyang Liu[a,b,*], Richard Barker[a,b], Chun Wang[a,b], Jiong Qian[b,c], Anne Neville[a,b] and Frederick Pessu[a,b].

a. Institute of Functional Surface, School of Mechanical Engineering, University of Leeds, Leeds, LS2 9JT, United Kingdom.
b. Jiuli Corrosion and Integrity Centre Laboratory (University of Leeds), Leeds, LS2 9JT, United Kingdom.
c. Engineering Research Centre of High-Performance Nuclear Power Pipe Forming of Zhejiang Province, Huzhou 313028, China

* Corresponding author: Qingyang Liu; Email: mnql@leeds.ac.uk

Keyword:

Molten salt; Thermal cycling; Stainless steels; Ni-based alloys; Multi-corrosion layer.

Highlight:

- **Intermittent cooling effect during thermal cycling significantly influences the corrosion behaviour of alloys in Ar.**
- **Thermal cycles in Ar was observed to reduce CR compared to isothermal conditions.**
- **Ni-based alloys show better corrosion resistance than SSs at any conditions.**

Abstract:

Molten nitrate salts are widely used as heat transfer fluids and heat storage media for concentrated solar power (CSP) plants due to their favourable thermo-physical properties. The corrosion of alloys in nitrate salts used in CSP plants poses a critical challenge to the safety, cost and efficiency of their operations under high temperature. In this study, the corrosion behaviour of stainless steels; 321 and 347, and Ni-based alloy; IN 625 and In 825, in Solar (nitrate) salts has been experimentally investigated under isothermal (at 600 °C) and thermal cycling (between 600 °C and 250°C) conditions, and under argon atmosphere. Corrosion assessment of test materials was achieved using gravimetric measurements in a simulated metal – molten salt environment in a furnace for 7 days. The micro-morphology and cross-sectional analysis of the corroding interface was carried out using a combination of scanning electron microscopy, energy dispersive X-ray spectroscopy and X-Ray diffraction techniques. Compared with isothermal condition, thermal cycling between the 250°C (for 12 hrs) and 600°C (for 12 hrs) reduces the corrosion rate of test materials, the severity of corrosion attack and the thickness of corrosion product layers. The result also shows that corrosion product

breakdown due to spallation was also reduced by lower time at maximum temperature and cooling effect during thermal cycling, especially in stainless steels when compared with isothermal conditions at 600°C. The spallation process became prominent with the formation of a Na-Fe oxide layer at the corrosion interface. Ni-based alloys show better corrosion resistance than stainless steels under both isothermal and thermal cycling conditions due to the superior passivation behaviour from combined Cr and Ni enrichment. Cr_2O_3 and NiO were formed as an inner layer in a multi-layered corrosion products on the metal surface from reaction with oxygen. Oxygen was made available from the decomposition of nitrate ions at 600°C.

Introduction

With the rapid growth of world's population, increased industrialisation of emerging economies, the limitation of conventional and non-renewable energy sources, and the established impact of fossil fuel on global warming, there is a strong motivation to explore alternative and renewable sources of energy (Walczak et al., 2018). Compared with other renewable resources (e.g. wind, geothermal and tidal), solar energy has shown great promise due to the abundant amount of energy reaching the Earth (Pelay et al., 2017; Walczak et al., 2018). According to some estimates from International Energy Association, the optimally harnessed solar energy alone can meet the total global energy demand (Alva et al., 2018). Electricity generation from solar irradiation is achieved by photovoltaic (PV) and photothermal conversion (Desideri and Campana, 2014), Compared with photovoltaic technologies, concentrating solar power (CSP) has gained particular interest for large scale applications due to its advantage in terms of potential efficiency, low operation cost and low environmental impact. It also has the advantage of being able to integrate thermal energy storage (TES) systems (Alva et al., 2018) to mitigate the intermittence of power supply. In CSP systems, molten salts (especially mixture of $NaNO_3$ and KNO_3) are currently widely used as heat transfer fluids (HTF) and sensible heat storage materials to collect, transfer and store energy in heat collectors, heat transfer pipes and hot tanks, respectively. This inevitably poses significant threat to all the metallic components, which are exposed to molten salts at extremely high temperature gradients (typically ranging from 550 - 850°C) (Bell et al., 2019) and are more vulnerable to high temperature fatigue and intergranular corrosion (IGC) at the metal-salt interface.

Considering the potential for corrosion to occur, the optimal combination of molten salt and metallic materials is critical for mitigating the risk of catastrophic failure of metal components used in CSP plants. Stainless steels and Ni-based alloys are widely used in CSP plants due to their good mechanical properties, high corrosion resistance and oxidation resistance. Ni-based alloys have overwhelming superiority in relation to resistance to pitting corrosion, crevice attack and stress corrosion cracking compared with stainless steels (Walczak et al., 2018).
Therefore research that helps to develop and improve the understanding of metal molten salt interactions is needed to mitigate molten salt induced material degradation in CSP plants. This has not received the required research attention to date, particularly research under thermal cyclic stress. A summary of corrosion studies on molten salt (solar salt) corrosion is shown in Table 1. The focus of some of these studies are on the effect of temperature and molten salt

chemistry on the corrosion rate of the selected alloys. It was shown that AISI 321 exhibited increasing corrosion rate from 1 to 460 μm/year as the temperature increased from 400 to 680 °C (isothermal) with the largest increase in corrosion rate occurring between 600 and 680°C from 15.9 to 460 μm/year, respectively (Kruizenga et al., 2013) (Gomes et al., 2019). Similar trend was also found for Ni-based alloy in solar salt (Kruizenga et al., 2013). Bradshaw (Bradshaw and Goods, 2001b) first started thermal cycling test in air with a 7.5-hour hot and 0.5-hour cold cycle and found that thermal cycling moderately increased the corrosion rate of three stainless steels compared with isothermal condition. This methodology cannot simulate the real condition for CSP which includes day-time heating and night-time cooling. The results presented by Bradshaw (Bradshaw and Goods, 2001b) mainly focused on characterising the corrosion rate and corrosion layer without providing persuasive evidence to explain the increase in corrosion rate due to thermal cycling.

Openly available studies on corrosion behaviour of alloys in molten-salt mixtures under inert atmosphere and thermal cycling conditions are very limited. This study focuses on thoroughly investigating the corrosion performance of two stainless steels and two Ni-based alloys under isothermal and thermal cycling conditions. Argon was chosen as an inert protective atmosphere to minimise the influence of unwanted O_2 gas on corrosion behaviour, and isolate and characterise the true effect of thermal cycling. The test protocols were developed to closely simulate real solar power tower from the industrial scale CSP that accounts for conditions during 12-hour day-time heating and 12-hour night-time cooling in heat transfer pipes or heat storage tanks. The results and findings in this study could provide a new theoretical basis and guidance for the characterisation and selection of the materials with molten salt in CSP plants.

Table 1: summary of corrosion data for alloys in solar salt under isothermal and thermal cycling condition. ('ISO' indicates isothermal corrosion, 'TC' indicates thermal cycling, 7.5 hours immersion in molten salt at maximum temperature and 0.5-hour cooling in ambient air at 95°C, for a total cycle time of 8 hours))

Author and Ref	Alloy	Molten Salt	Temperature (°C)	Exposure time (h)	Corrosion rate (μm/year)
(Goods and Bradshaw, 2004)	304	Solar salt	570-ISO	7008	7.9
(Bradshaw and Goods, 2001b)		Solar salt+0.05% NaCl	565-ISO	4584	11.5
		Solar salt+0.05% NaCl	565-TC	4432	15.6
(Goods and Bradshaw, 2004)	316	Solar salt	570-ISO	7008	9.4
(Bradshaw and Goods, 2001b)		Solar salt+0.05% NaCl	565-ISO	4584	8.96
		Solar salt+0.05% NaCl	565-TC	4084	10.72
(Bradshaw and Goods, 2001b)	316L	Solar salt+0.05% NaCl	565-ISO	4584	8.41
		Solar salt+0.05% NaCl	565-TC	4084	12.2
(Kruizenga et al., 2013) & (Gomes et al., 2019)	321	Solar salt	400-ISO	3064	1.0
			500-ISO	3064	7.1
			550-ISO	3064	9.0
			600-ISO	3064	15.9
			680-ISO	3064	460

(Kruizenga et al., 2013)	347	Solar salt	400-ISO	3064	0.7
			500-ISO	3064	4.6
			600-ISO	3064	10.4
			680-ISO	3064	447
(Kruizenga et al., 2013)	IN 625	Solar salt	400-ISO	3064	0.17
			500-ISO	3064	1.8
			600-ISO	3064	12.7
			600-TC	3200	21.7
			680-ISO	3064	554

Experimental system description

Experimental material

The materials used in this study were AISI 321, AISI 347 austenitic stainless steels, and Ni-based Inconel 625 and Incoloy 825 alloys. The composition of these alloys is provided in Table 2. The as-received pipes were supplied by Zhejiang JIULI Hi-tech Metals Co., Ltd China. Samples of approximately 1 cm^2 area were obtained from seamless pipes as shown in Figure 1. They were first wet-ground using silicon carbide (SiC) paper up to 2000 grit and followed by polishing with 9 μm, 6μm, 1μm and 0.25 μm diamond suspension. Polished samples are then degreased with acetone before commencement of experiments. The initial dimensions and mass of coupons were recorded using and analytical balance. The samples for cross-section analysis were embedded in epoxy resin before being abraded and polished. Prior to cross-section analysis, the prepared samples were sputtered with Ir to enhance the conductivity of the specimens.

Solar salt (60 wt.% $NaNO_3$ and 40 wt.% KNO_3) is the most common molten salt used in CSP plants(Walczak et al., 2018) and therefore was selected for this study. The solar salt used was purchased from Shanghai Chemical Reagents Limit Company with analytical reagent purity as shown in Table 3 (from supplier data). The salts were weighed to achieve the required ratio and separately dried at 120°C for 24 h in a furnace, heated at 300°C for 24h to achieve a homogeneous mix of salt before the experiments.

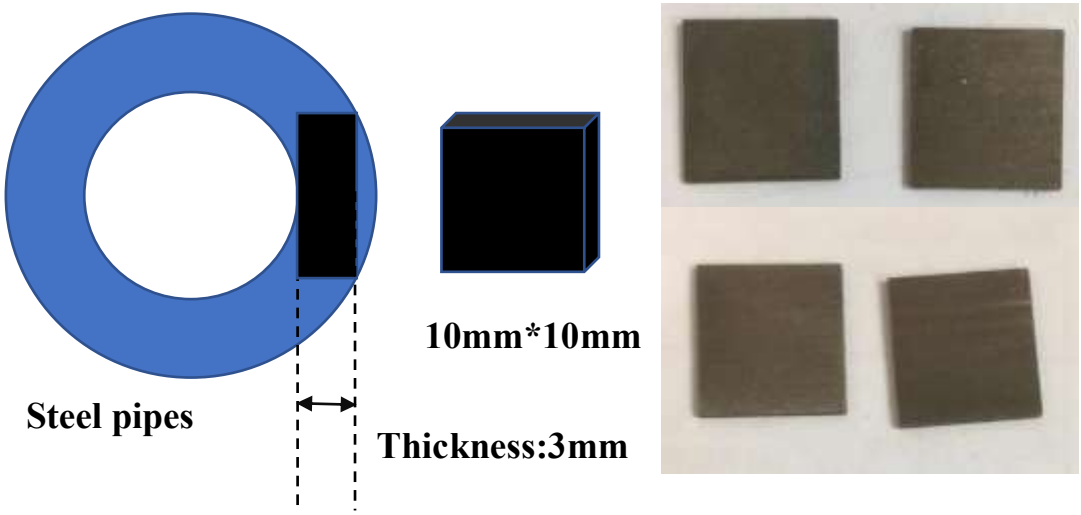

Figure 1: Geometry of samples obtained from the pipes and the dimensions.

Table 2: Alloy composition of 321 and 347, IN 625 and In 825 (wt%).

Alloy	C	Mn	Si	P	Cu	Cr	Ni	**Ti**	**Nb**	Mo	**Fe**
AISI 321	0.018	1.44	0.519	0.035	-	17.33	9.24	0.225	-	-	Bal.
AISI 347	0.049	0.95	0.402	0.026	0.11	17.35	9.65	-	0.656	-	Bal.
IN 625	0.018	0.04	0.142	0.001	0.03	21.69	62.36	0.211	3.31	8.65	3.06
In 825	0.008	0.67	0.258	0.0119	1.75	22.6	40.18	0.943	0.025	2.88	30.32

Table 3: Main component contents and purity of the test salt (wt%), from supplier data.

Components	KNO_3	$NaNO_3$
Main component, %	99.0	99.0
Insoluble, %	0.004	0.004
IO_3^-, %	0.0005	0.0005
SO_4^{2-}, %	0.003	0.003
NO_2^{2-}, %	0.001	0.0005
Ca, %	0.004	0.005
Fe, %	0.0002	0.0001
Mg, %	0.002	0.002

Specimen preparation and test procedure

A tubular furnace was used to provide a stable and accurate high temperature environment with argon atmosphere. Figure 2 shows the photo of the furnace and basic assembly drawing of the oven. In this test, the sample-containing crucibles are placed in the middle of the tube and the preparation procedure are as follows.

Four specimens of each alloy were placed horizontally in each Al_2O_3 crucible in order to ensure the same contact surfaces between the specimens and the molten salt. The homogeneous solid salts were poured into each sample-containing crucible before being transferred into the furnace to dry under argon atmosphere for 12 hours at 180°C. The furnace is gradually heated up to test temperature, with the test commencing when the test piece temperature exceeds 97% of the desired test temperature. It should be noted that the test chamber was filled with inert argon gas in this study.

In order to investigate the corrosion behaviour of test samples under thermal cycling conditions, tests were initially performed at a constant temperature of 600°C for isothermal corrosion. Under thermal cycling conditions, the temperature was controlled to fluctuate between 250 and 600°C, representing peak-time heating of molten salt and night-time cooling of molten salt in CSP storage tanks and flow lines. The selection of duration of exposure of materials to molten salts in these configurations are designed to replicate as closely as possible the real-time cycle between daytime 12-hour heating and night-time 12-hour cooling. The temperature range to be explored were chosen based on the melting point at 220°C and stability limit at 600°C for the molten salt (solar salt). The thermal cycling profile are shown in Figure 3.

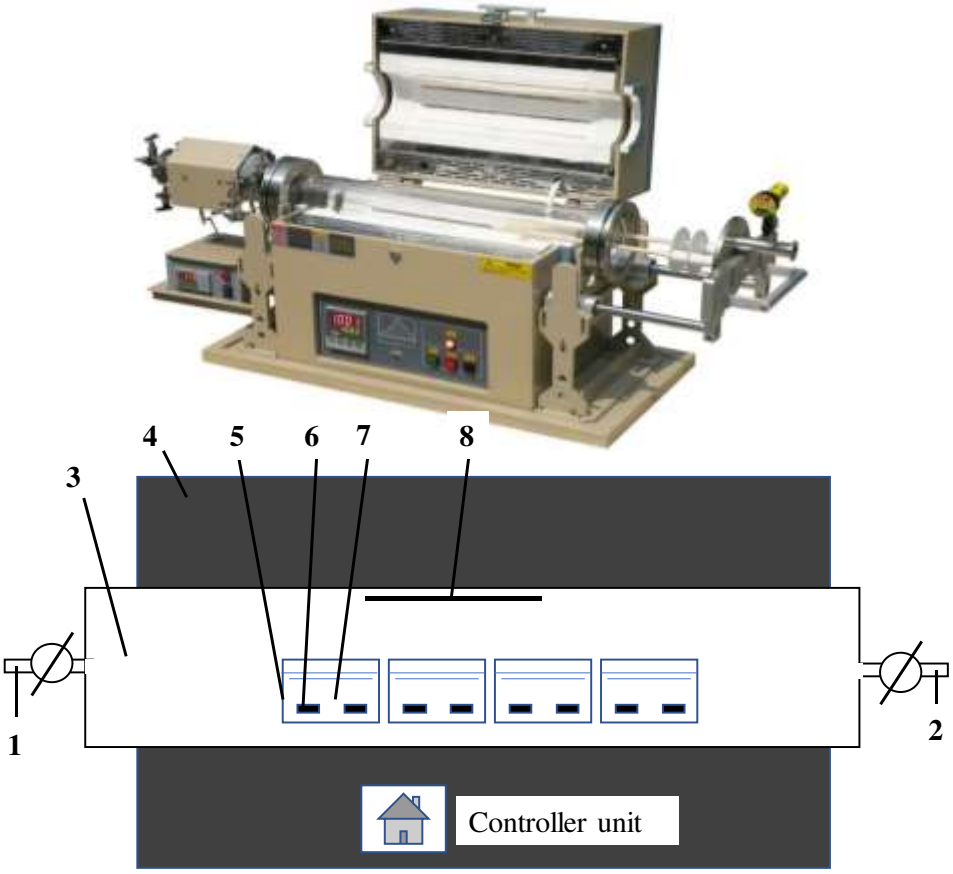

Figure 2: The structure of tubular furnace whole and part. 1-gas inlet; 2-gas exit; 3-test chamber; 4-heating unit; 5-crucible; 6-specimen; 7-molten salt; 8-thermocouple.

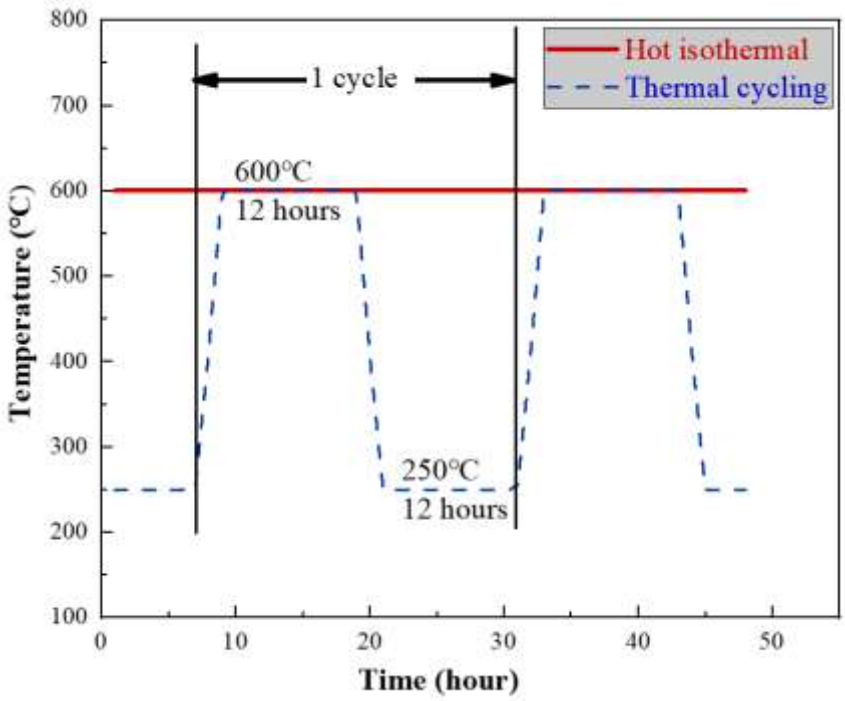

Figure 3: Time-temperature profile of isothermal immersion and thermal cycling (heating and cooling rate at 10°C/min with 35-minute interval)

Mass loss measurement and corrosion rate calculations

After completion of the test and cooling process, the specimens were retrieved and cleaned ultrasonically in deionised water and alcohol to remove the residual salt. Three of four specimens were used in mass loss test and the fourth specimen was used to characterise the corrosion products using techniques such as Scanning Electron Microscope (SEM), Energy Dispersive Spectrometer (EDX) and X-ray diffraction (XRD) and other morphology and composition characterisation tests. The specimens were then dried and weighed to obtain the mass changes using an analytical balance with 0.01mg precision.

As described in ASTM G1-03 (G1-03, 2017) and British standard (BS EN ISO 8407:2014), the coupons were descaled to remove the corrosion product using a standardised procedure of 2-min washing with 10% H_2SO_4 at 20-25°C and 20-min washing with 10% HNO_3 at 60°C for Ni-based alloys and austenitic stainless steels, respectively(G1-03, 2017). After removal of corrosion product, the samples were weighed.

Weight changes before and after the corrosion test were used to estimate the corrosion rate via the **Equation 1** and **Equation 2**, assuming uniform corrosion:

$$\frac{\Delta m}{S} = \frac{m_0 - m_1}{S} \qquad \textbf{Equation 1}$$

$$CR(\mu m/y) = \frac{87600\ \Delta m}{\rho\ S\ t} \qquad \textbf{Equation 2}$$

Where m_0 and m_1 represent the weight of specimen before and after corrosion, respectively. $\Delta m/S$ is descaled mass loss per unit area (mg/cm^2), ρ is alloy density (g/cm^3): the density of AISI 321, 347, IN 625 and In 825 are 7.94, 8.03, 8.14 and 8.14 g/cm^3, respectively. t is the immersion time (h). The mass loss data was determined based on the average of three measurements per sample to ensure accuracy.

Microstructure analysis and surface characterisation

A Bruker D8 X-ray diffractometer was used for X-ray diffraction analysis of alloys to identify the corrosion product on the surface using monochromatic Cu Kα radiation (λ=1.5418 Å). XRD patterns were collected in the 2θ range from 10° to 90° with a 1.5°/min scan rate. The surface morphology and cross-sections analysis of samples were investigated using a Zeiss optical microscope (OM) (Axio Imager 2) and Carl Zeiss EVO MA15 scanning electron microscope (SEM). The SEM was integrated with an Oxford Instruments Aztec Energy dispersive X-ray (EDX) system with an 80mm X-max SDD detector which provided secondary and backscattered imaging, EDX elemental mapping and line scans. The incident beam voltage of 20 keV was employed and working distance of 12–13 mm.

Results and discussion

Mass loss measurements

Results from mass loss measurements of AISI 321, AISI 347, IN 625 and IN 825 after 7 days immersion are shown in Figure 4. Mass change was measured after deionised water sonication and acid washing in turn. Ultrasonic washing with deionised water was used to remove the remaining salt and loose oxides on the sample surface (Hua et al., 2019). Corroded samples were taken to acid washing to remove all corrosion products and the subsequent mass loss measured was used to compute the corrosion rate according to the ASTM G1 standard. Referring to Figure 4, both stainless steel samples exhibited higher total corrosion rates than Ni-based alloys in both isothermal and thermal cycling immersion experiments. The corrosion rate of AISI 321 and 347 are 434 μm/y and 317 μm/y after 7 days from isothermal immersion tests, respectively. These values are 3-4 times higher than that of IN 625 and In 825 under the same conditions. Thermal cycling resulted in lower corrosion rate values of up to 25 – 50% than the corrosion rate from isothermal immersion tests for both stainless steels and nickel alloys. Thermal cycling between 600 and 250°C reduced the corrosion rate to 57.7 μm/y in IN625 from 128 μm/y after isothermal tests, and to 124 μm/y in AISI 347 from 317 μm/y after isothermal test. Mass change measurements after ultrasonic washing consistently show mass gain for samples from thermal cycling experiments while samples from isothermal experiments show mass loss. This is an indication of higher material loss rate from isothermal tests and improved protective properties from oxide layers formed under thermal cycling conditions. Under isothermal conditions, it has been reported that a high initial corrosion rate is needed to drive the initial formation of dense corrosion product layers (oxide layers). This could either protect the metal substrate or easily undermined it with extended experiment time to promote a transition from dense oxide layers to loose/porous oxides(Bell et al., 2019). The latter can be linked to sustained molten salt – metal interaction at a high temperature of 600°C.

The higher corrosion rate from isothermal tests than from thermal cycling tests is mainly linked to the lower time (12 hours per 24 hours experiment time) at maximum temperature of 600°C under thermal cycling conditions. This is due to the effect of the 12 hours of cooling process per thermal cycle. Under isothermal condition, the continuously formed oxide layers have more potential to breakdown and spall off due to the instability of the layers at high temperatures (Encinas-Sánchez et al., 2019). The sustained period of thermal effects under isothermal conditions is substantially tempered by intermittent cooling process under thermal cycling conditions over an interval of 12 hours per cycle. This period of cooling is long enough to limit the potential impact of thermal fatigue linked to thermal shock and reduce the impact of thermal cycles on the integrity of oxide layers. The corrosiveness of the molten salt system is also continuously and progressively increased by the decomposing nitrate salt into nitrite and oxide ions (Walczak et al., 2018) with longer residence time at 600 °C, resulting in higher corrosion rate and oxide formation. The process of molten salt decomposition also takes place under inert gas atmosphere as is the case in this study (Bonk et al., 2020). The outwards diffusion of alloy elements from the base material to form oxides at the molten salt-metal interface is also promoted by high temperature (in this case, 600°C) and duration (Bataillou et al., 2018). This

is sustained under isothermal conditions but interrupted under thermal cycling conditions to limit material loss rate. Based the statements above, under the thermal cycling conditions explored in this study, the range of temperature used for the cooling phase and the long residence time during this period is believed to help to slow down the kinetics of outward diffusion active atoms of key alloying elements in the base material, corrosion oxide formation and breakdown, thereby reducing material loss rate. The intermittent cooling effect during thermal cycling could also provide a way of limiting the progressive increase in the corrosiveness of molten salt linked to the thermal stability of molten salts at high temperature. This indirectly helps to improve the adherence of initially formed corrosion oxide layers at 600°C under thermal cycling conditions. This has been shown to restrict the potential transformation from dense oxide layers to loose/porous oxide layers, and detailed evidence and analysis are discussed after.

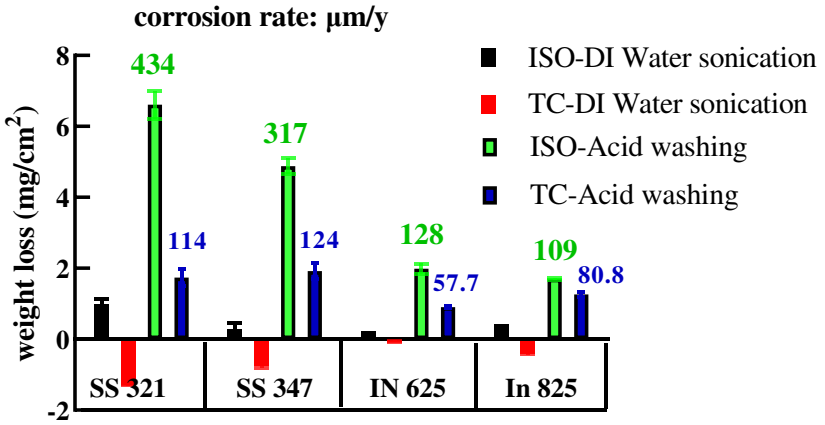

Figure 4: Mass loss (and corrosion rate) of AISI 321, AISI 347, IN 625 and In 825 specimens under isothermal and thermal cycling in solar salt for 7 days

2-week thermal cycling test as extra data

Considering to different immersion time at 600 ˚C between 1-week isothermal with 1-week thermal cycling, 2-week thermal cycling test in argon have been performed to better explain and understand the synergic effect of thermal cycling and immersion temperature time at maximum temperature on the corrosion mitigation process. A two week thermal cycling experiment represents an equivalent of 1 week Isothermal test at 600°C and additional 1 week Isothermal test at 250°C in argon. Referring to Figure 5 the weight loss of alloys from thermal cycling tests (between 600°C and 250°C) after 14 days is slightly (~ 1.5 times) higher than that after 7 days, but much lower than alloys from isothermal tests at 600°C after 7 days (except for In 825). Comparing the results after continuous and intermittent 7-day immersion at maximum temperature, the cooling process during thermal cycling is clearly central to the overall corrosion behaviour of the alloys.

Compared with the isothermal and thermal cycling tests after 7-day immersion, higher corrosion rate recorded from isothermal test was due to consistent exposure at maximum temperature of 600°C. If we introduce the test results from 2-weeks thermal cycling test with an equivalent of 1-week isothermal exposure at 600 ºC, corrosion rate data in Figure 5 is a clear evidence that the intermittent cooling for an equivalent of 1 week isothermal exposure at 250°C helps to retard the corrosion and corrosion product kinetics.

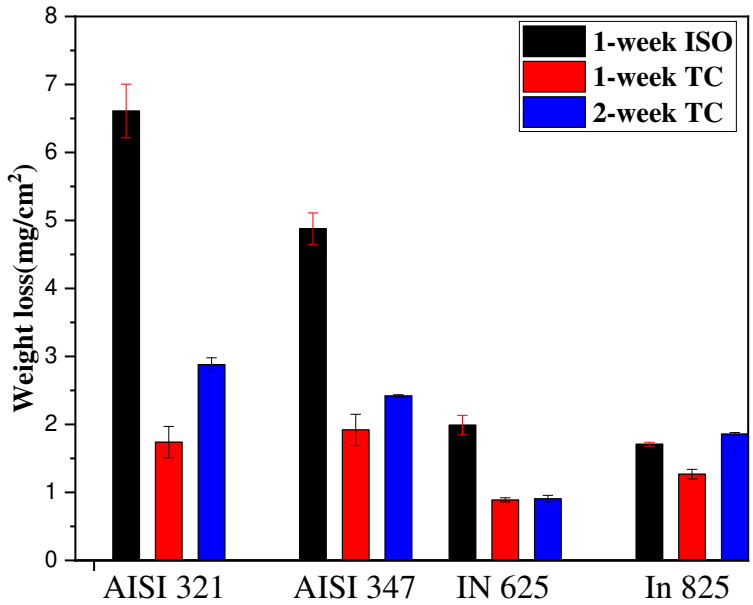

Figure 5 Weight change of 7-day isothermal and thermal cycling and 14-day thermal cycling samples after acid washing (in mg/cm^2)

Post-experiment salt characterization

Except from the thermal effect on the samples itself, the aggressiveness of salt system need to be checked after different test conditions to figure out how the salt chemistry change influencing the corrosion degradation of material.

In relation to the salt chemistry, X-ray Diffraction patterns of the salt before and after 7-day isothermal and thermal cycling test are presented in Figure 6. The as-received salt was identified as only mixture of (Na, K) NO_3, while the salts after Isothermal and thermal cycling immersion tests showed peak of (Na, K) NO_2 around 30.001 (100 % intensity) degree and 32.065 degree (55% intensity, according to Reference code 00-006-0392). This indicates the presence of nitrites in the form of (Na, K) NO_2 from the decomposition of (Na, K) NO_3 after 7-day immersion. It's worth noting that the peak at 32.065 degree (not main peak for $NaNO_3$ with 14% intensity and main peak for $NaNO_2$ (6000 a.u.) with 55% intensity) in Figure 6 (b) for 1 week isothermal test shows higher intensity (0-2000 a.u.) than that in Figure 6 (a), (c) and (d) for as received, 1 week and 2 weeks thermal cycling test respectively. Other researchers (Han et al., 2021) also reported that the $NaNO_2$ was found in Solar salt after 500 thermal cycles, thus influencing the thermal physical properties of molten salt. The reported (Han et al., 2021) XRD patterns of thermal cycled salt show agreement with the results in our study. This supported results published by Bonk. (Bonk et al., 2020), which shows that the chemistry of nitrate salts changes to produce nitrite in a nitrate-nitrite ratio of 94-6% after isothermal test at 600 ºC in a closed atmosphere the ratio will keep stable with increasing immersion time. This is a clear evidence to confirm that the salt aggressiveness after 1-week isothermal is higher than that even after 2-week thermal cycling due to increase in nitrite concentration from solar salt decomposition. The detailed comparison of peak intensity of $NaNO_2$ after different test conditions are shown in **Table 4**.

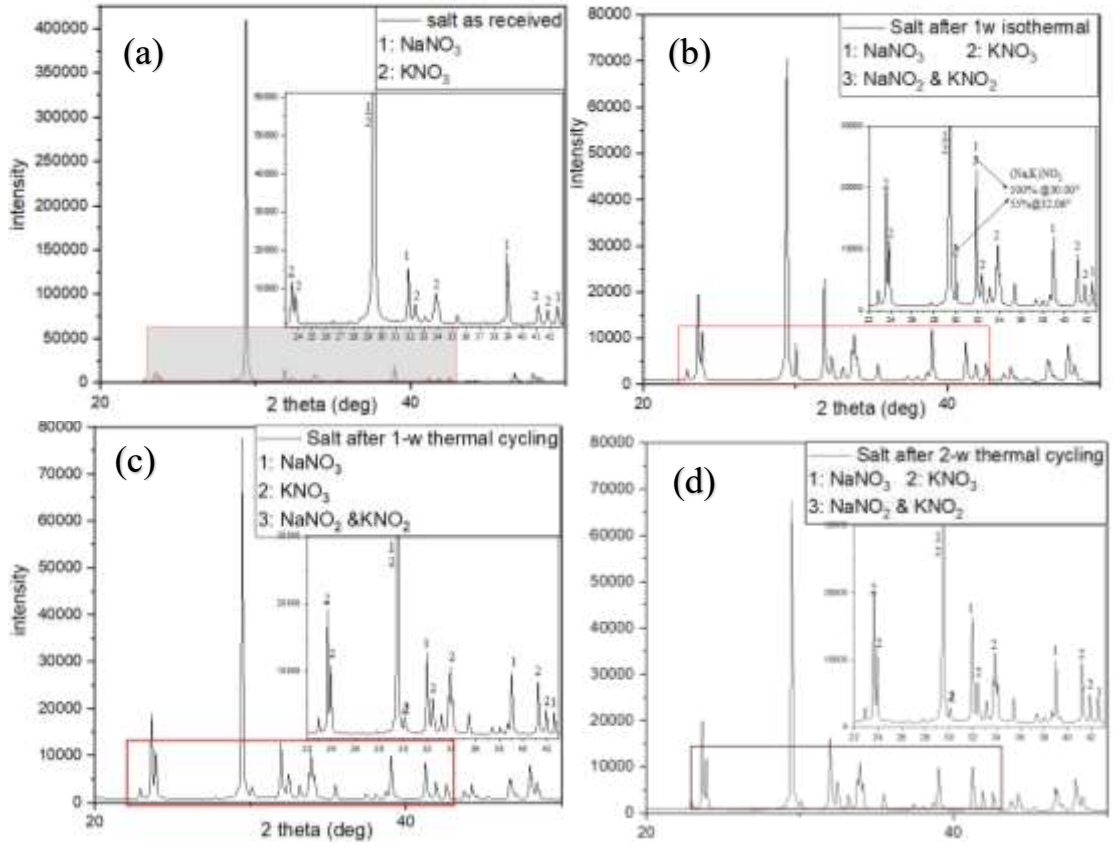

Figure 6 XRD results of solar salt before and after immersion test, (a) as received; (b) after 1-week isothermal; (c) after 1-week thermal cycling and (d) after 2-week thermal cycling (Reference code 00-006-0392, 00-036-1474 and 00-05-0377)

Table 4: Main peaks intensity of $NaNO_2$

	$NaNO_2$ intensity at 30 2theta (100% intensity)	$NaNO_2$ intensity at 32 2theta (55% intensity)
As-received salt	0	0
1-week isothermal	9800	6000
1-week thermal cycling	3200	0
2-week thermal cycling	3500	2000

Corrosion product characterisation

XRD analysis

Figure 7 (a) (b) (c) and (d) show the XRD patterns of the corroded surface of AISI 321, AISI 347, IN 625 and In 825 after 7-day immersion in Solar salt under isothermal and thermal cycling condition, respectively. Referring to the XRD patterns, it is confirmed that the oxide layers formed on the surface of AISI 321 and AISI 347 in solar salt are iron chromium spinel ($FeCr_2O_4$), iron oxide (Fe_2O_3), and a less dense, and less protective layer of sodium ferrite ($NaFeO_2$). Nickel oxides formed on the corrosion surface of Ni-based alloy, as well as iron chromium spinel and iron oxide, shown in Figure 7 (c) and (d). Compared with the products formed on IN 625 samples, more types of iron oxide mixtures were found on the surface of In 825 due to its

higher iron content and lower nickel content. These results have a good agreement with those observed from SEM images and EDX analysis presented later.

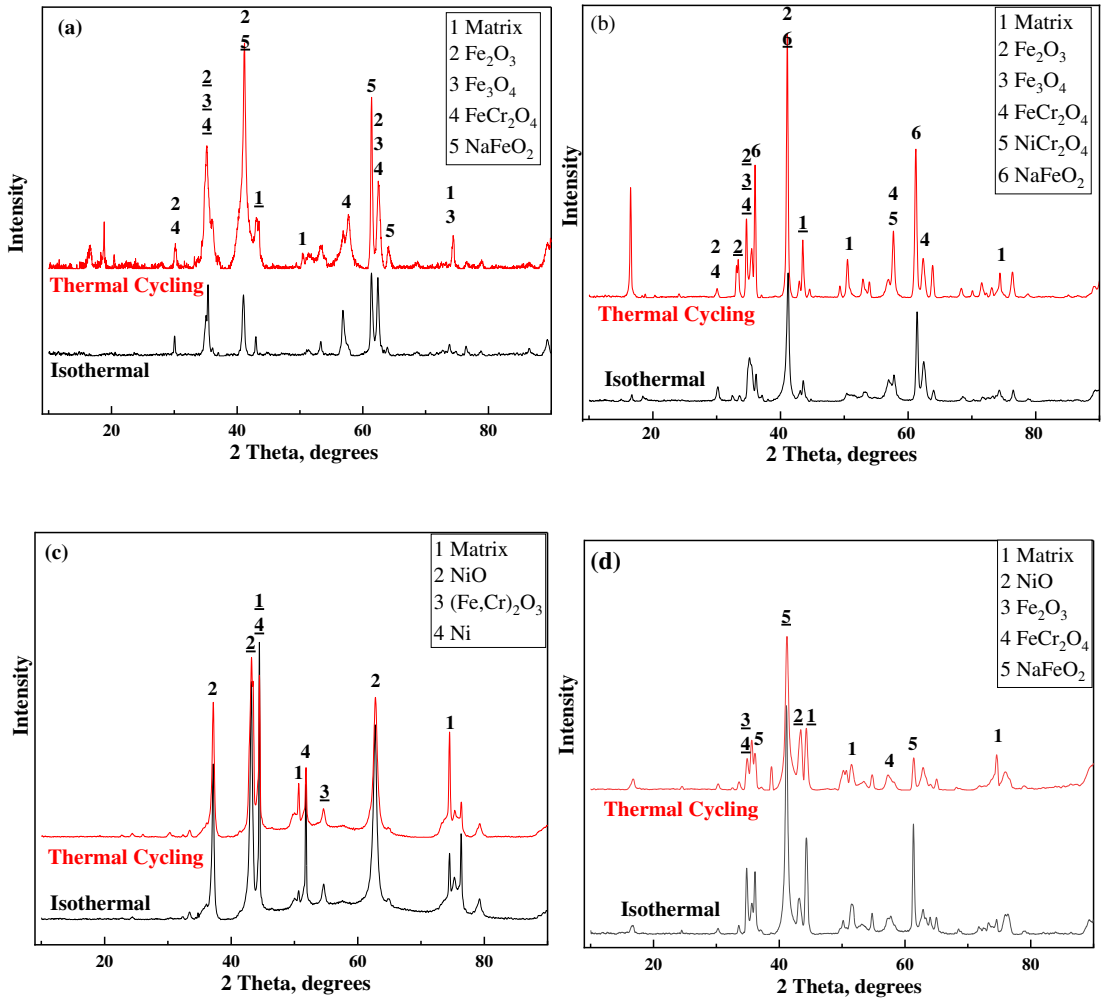

Figure 7 XRD patterns of (a) AISI 321; (b) AISI 347; (c) IN 625 and (d) In 825 after isothermal and thermal cycling immersion in solar salt for 7 days (Reference code for Fe_2O_3: 00-039-1346, NiO: 04-013-0889 and $FeCr_2O_4$: 01-080-6393 are corresponding to the standard pattern from JCPDS Committee (Encinas-Sánchez et al., 2020; Gates-Rector and Blanton, 2019)

SEM surface analysis

Each corroded sample surface was examined using SEM to characterise the properties of the corrosion products layers. This is shown in Figure 8. The complimentary EDX results is provided in Table 5. Referring to Figure 8, the corrosion products from isothermal and thermal cycling experiments on stainless steel samples show distinct properties. As shown in Figure 8 (a1) and (a2) for AISI 321 samples after isothermal tests, loose corrosion products appear to have spalled off due to the poor cohesion/adherence to bulk material. The Ni and Cr rich areas are confirmed to be the fresh metal by the EDX mapping and data shown in Figure 8 a1. After spallation of the loose oxide layer, large areas of fresh metal were directly exposed to molten salt, resulting in grain boundary attack in these locations. The dark deposit in region A-1 was confirmed as Al_2O_3, whereby the Al has come from the alumina crucible. The product within region A-6 was identified as $NaFeO_2$ and Fe_2O_3, which are also identified as the primary

corrosion products on the surface of samples from thermal cycling experiments in Figure 8 (a3) and (a4) (region A-3, 4, 5). A more protective inner layer of $FeCr_2O_4$ (Fe-Cr spinel region A-2) and a Cr-enriched layer were identified in Figure 8 (a3) after spallation of sodium-iron oxides on test samples form thermal cycling experiments. Figure 8 (b1-b2) and (b3-b4) show the corrosion surface of AISI 347 after isothermal and thermal cycling immersion test, respectively. Non-protective porous oxide layer was observed in region B-1, B-2 and B-4, and believed to be iron oxide and sodium ferrite form EDX data analysis in Table 5. It is evident from Figure 8 (b1 and b2) that the iron oxide and sodium ferrite is non-adherent and easily detachable during the test (see region B-3 in Figure 8 b1). Sodium ferrite and iron oxide were also found on the surface of thermal cycled AISI 347 samples. They are formed as dispersed and porous layers across the corroding surface without no evidence of spallation, as shown in Figure 8 (b3-b4). The spallation behaviour of corrosion products on stainless-steel surfaces has been reported by several researchers (Bradshaw and Goods, 2001b; Gomes et al., 2019; Stott and Wei, 1989; Trent et al., 2016), and attributed to the stress due to the mismatch of thermal expansions and Young's modulus between the bulk steel and corrosion scales. Referring to Ni–based alloys, the corrosion products formed are more uniform with a consistent distribution of elements across the corrosion surface (see Table 5) for samples from isothermal and thermal cycling experiments. Samples from isothermal tests exhibited larger crystals of corrosion products as shown in Figure 8 (c1) and (d2) for IN 625 and In 825 respectively, when compared with corrosion products formed under thermal cycling condition in Figure 8 (c3) and (d4) for IN 625 and In 825, respectively. The main corrosion products of IN 625 is believed to be NiO from EDX data in Table 5. NiO is known to be protective as shown by the corrosion rate data in Figure 4. The SEM images in Figure 8 (d1-d4) also shows that the protectiveness of NiO is also linked to how well adhered it is to the substrate alloy at 600°C (Soleimani Dorcheh et al., 2016). The EDX data also shows evidence of the potential for mixed oxide of Fe, Cr and Ni being formed as corrosion products on the corroding surface of In 825.

The results presented clearly show that the corrosion rate recorded for stainless steel samples is always higher than Ni-based alloys under isothermal and thermal cycling conditions are due to the loose and porous properties of oxides formed on the stainless-steel surface. These oxides are less protective than NiO against the combination of chemical and redox activities from molten salt, and thermal stress. This induced stresses could be due to differences in the coefficient thermal expansion and elastic modules between the metal and oxide layers, causing cracking and spallation between protective oxides (Bell et al., 2019). Referring to the stainless steel samples, it is evident that more severe spallation occurs under isothermal condition than under thermal cycling conditions. The spallation behaviour of the oxide layers would certainly affect the protectiveness of corrosion layer, thus affecting the corrosion rate. However, the cooling effect of lower temperature during thermal cycling and the residence time of 12 hrs per cycle at test temperature is capable of tempering the thermal stress and help to lower corrosion rate after thermal cycling tests. It is also believed that this helps to improve the thermal stability and adherence of the oxide layers and to avoid spallation of protective dense corrosion layer. This is reflected in the higher corrosion rate and severer layer spallation in samples from isothermal tests than samples from thermal cycling tests in Figure 4 and Figure 8.

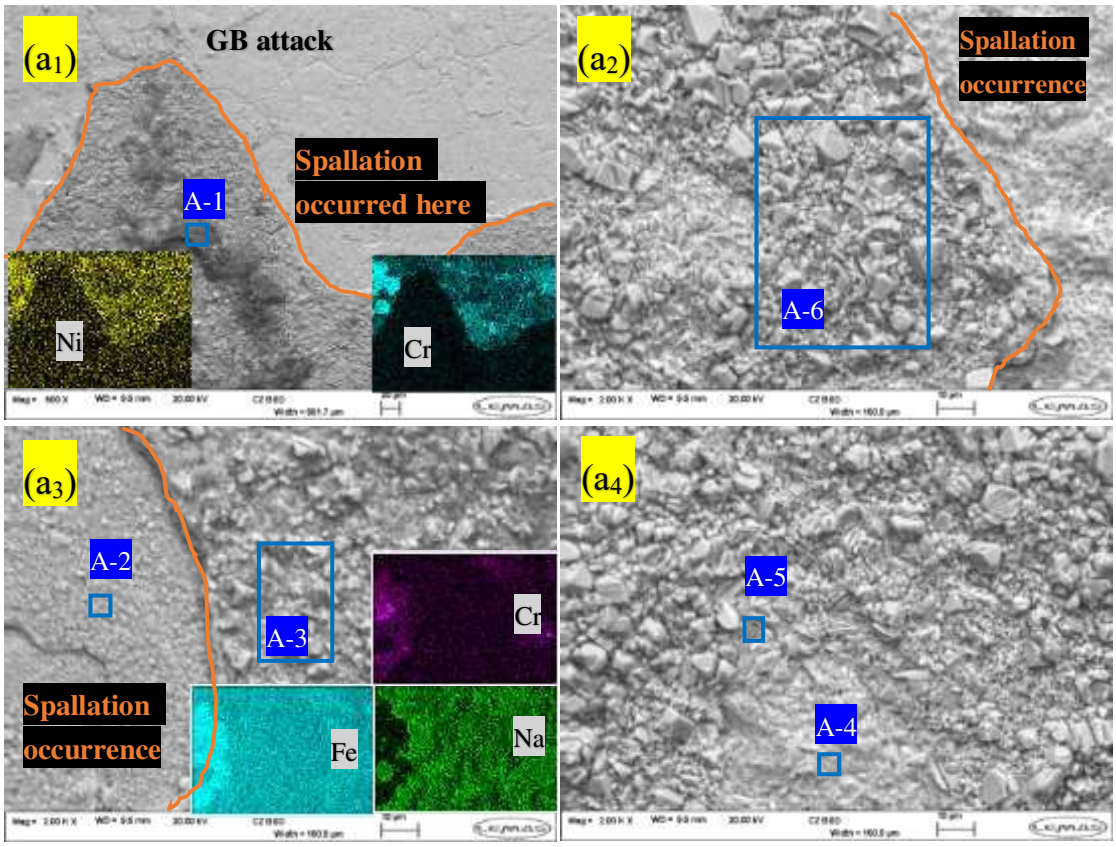
(a1)
GB attack
Spallation
occurred here
A-1
Ni
Cr
(a2)
Spallation
occurrence
A-6
(a3)
A-2
A-3
Cr
Spallation
occurrence
Fe
Na
(a4)
A-5
A-4

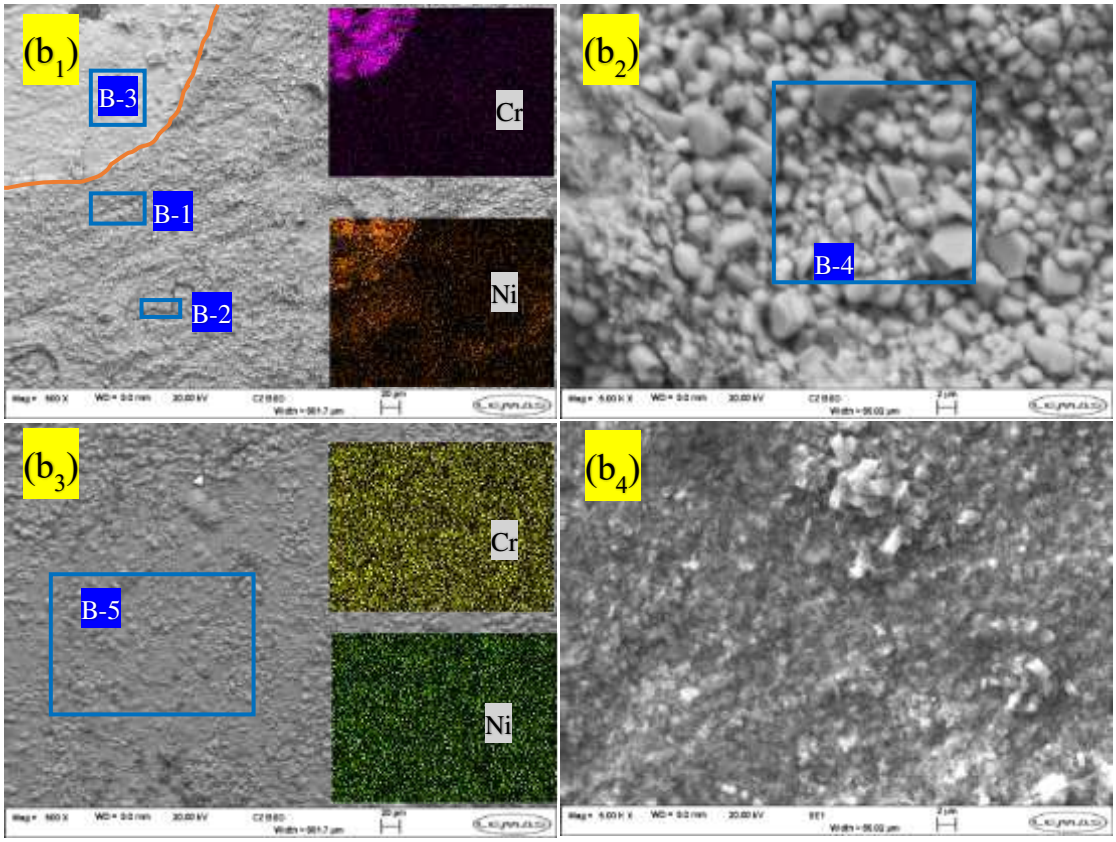
(b1)
B-3
Cr
B-1
B-2
Ni
(b2)
B-4
(b3)
Cr
B-5
Ni
(b4)

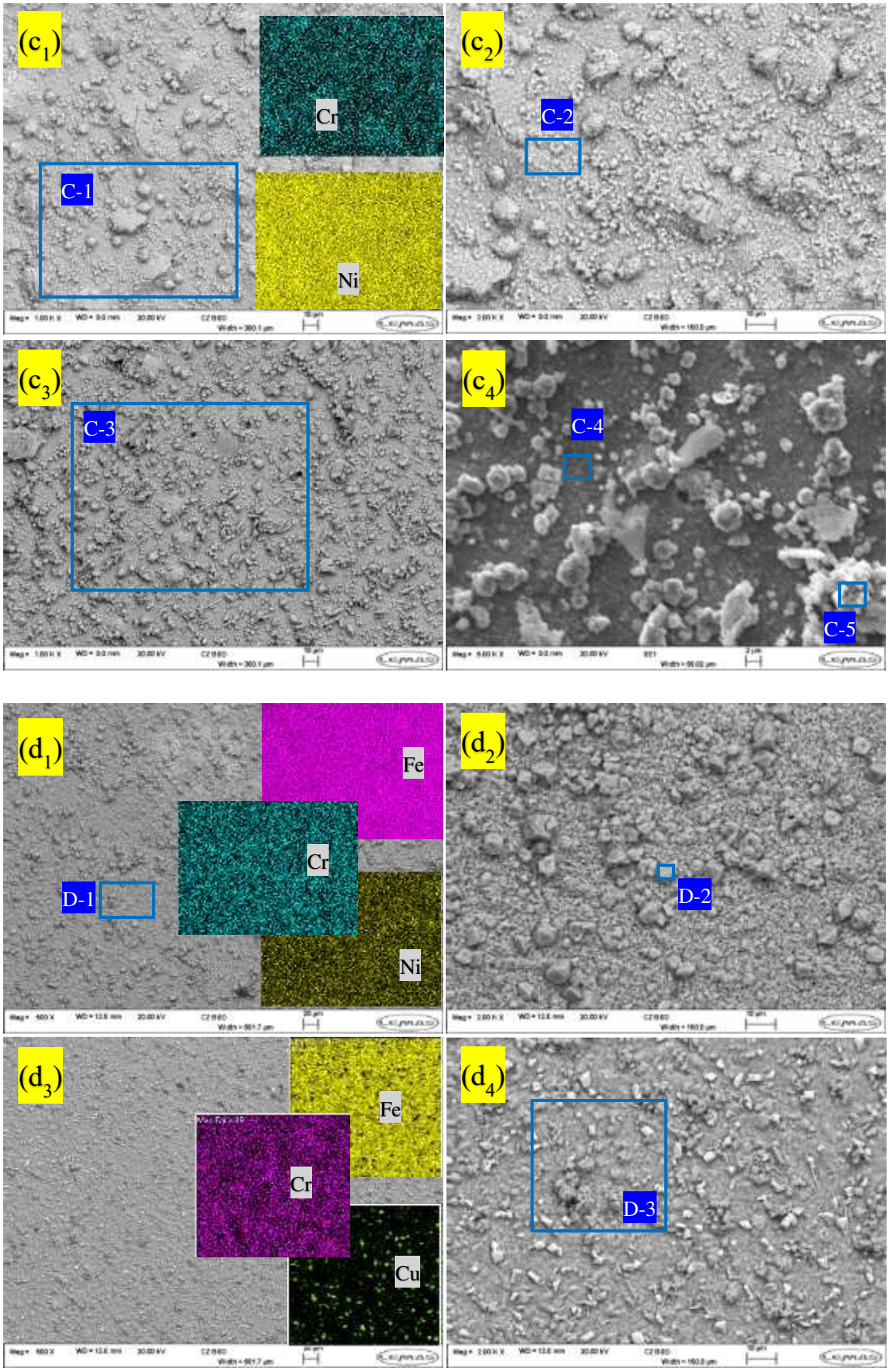

Figure 8: SEM top surface of the oxide scales formed on (a) AISI 321; (b) AISI 347; (c) IN 625; (d) In 825 after 7-day immersion test in solar salt; isothermal (1) (2) and thermal cycling (3) (4)

Table 5: EDX data for regions and possible phase in Figure 8.

Region (wt.%)	Possible phases	O	Fe	Cr	Na	Ni	other
A-1	Al_2O_3	57.94	1.88	0.17	1.48	-	22.72 Al
A-2	$FeCr_2O_4$, Fe_2O_3	28.97	48.36	8.13	0.99	1.19	1.03 Al
A-3	$NaFeO_2$, Fe_2O_3	32.8	43.25	0.86	8.37	0.36	0.74Al
A-4	$NaFeO_2$, Fe_2O_3	29.44	57.7	1.21	5.36	-	-
A-5	$NaFeO_2$, Fe_2O_3	26.06	66.2	1.05	6.53	-	-
A-6	$NaFeO_2$, Fe_2O_3	32.39	49.99	0.62	6.73	0.32	0.26Al
B-1	$NaFeO_2$, Fe_2O_3	29.86	50.64	0.62	9.99	2.99	-
B-2	$NaFeO_2$, Fe_2O_3	36.06	45.64	0.69	6.15	0.44	0.74Al
B-3	$FeCr_2O_4$, Fe_2O_3	28.78	51.29	8.52	1.43	4.71	-
B-4	$NaFeO_2$, Fe_2O_3	30.15	56.73	0.91	10.88	0.76	0.18Al
B-5	$NaFeO_2$, Fe_2O_3	30.5	41.25	1	10.03	0.68	0.53Al
C-1	NiO, $(Fe, Cr)_2O_3$	21.71	7.36	0.62	1.89	60.98	-
C-2	NiO, $(Fe, Cr)_2O_3$	21.53	7.45	1.1	2.08	60.86	-
C-3	NiO, $(Fe, Cr)_2O_3$	19.77	6.88	1.71	1.98	62.61	-
C-4	NiO, $(Fe, Cr)_2O_3$	14.88	4.57	1.08	1.66	70.93	-
C-5	NiO, $(Fe, Cr)_2O_3$	20.02	5.16	1.3	1.45	59.96	-
D-1	NiO, $NaFeO_2$, Fe_2O_3	31.77	43.54	1.25	10.17	5.17	0.55Cu
D-2	NiO, $NaFeO_2$, Fe_2O_3	34.19	39.6	1.04	9.11	6.78	1.14Cu
D-3	NiO, $NaFeO_2$, Fe_2O_3	32.74	40.63	1.34	7.43	3.8	4.49Cu

Cross-section analysis

Referring to the XRD and SEM results in Figure 7 and Figure 8, respectively, it is evident that different oxide layers were formed on the surface of alloys specimens after immersion test. The loose oxide layer of sodium-iron oxide spalls off during the test while others compounds with good adherence were shown to protect the base alloy against further molten salt–substrate alloy interactions. This section presents results from cross-section analysis using SEM-EDX techniques to provide detailed insight into the depth and mechanism of corrosion attack and interfacial oxide formation.

Figure 9 shows the cross-sectional images of AISI 321 samples after isothermal immersion tests. Continuous oxide layers presence is observed along the interface but with non-uniform oxide layer thickness across the interface as shown in Figure 9 (c). From the result of EDX line scan and mapping in Figure 9 (b) (d) (e), it is evident that the composition of the double corrosion layer included an outer 12 – 39 μm iron oxide layer and inner 13 μm iron/nickel chromium spinel layer. As shown in Figure 10, AISI 321 from thermal cycling tests shows uniform thickness of corrosion layer of about 10 μm along the interface, with 4.2 μm iron chromium spinel at the interface of layer/metal and 5.8 μm outer iron oxide layer. The reason of differences in the thickness of the outer iron oxide layer is the spallation behaviour of poorly adherent oxide layer formed from isothermal corrosion tests.

For AISI 347, a double oxide layer with thickness of 16 μm was formed on the surface of sample

from isothermal immersion tests. The double oxide layer is made up of 8 μm outer iron oxide layer and 8-μm inner iron chromium spinel layer as shown in Figure 11. Figure 12 presents the cross-sectional image of AISI 347 after 7-day of thermal cycling corrosion test. A corrosion product layer of thickness of 10 μm was found on the surface, comprising of an outer iron oxide layer and an inner layer of oxides of iron and chromium. A thin Ni enriched layer was observed at the alloy/oxide interface, which has been reported to be the result of the depletion of chromium from the bulk alloy (Kruizenga and Gill, 2014). No obvious spallation behaviour was found from the cross-sectional analysis of AISI 347 samples. The main difference between isothermal and thermal cycled samples are the formation of thinner corrosion layer and the presence of thin Ni-enrich layer after thermal cycling.

The cross section analysis of IN 625 after 7-day isothermal corrosion test at 600 °C is shown in Figure 13. The double corrosion product layer was formed as a continuous layer along the corrosion interface. However, this layer is not uniform across the corrosion interface, with thickness ranging from 9.5-16.5 μm. The inner layer was identified as a chromium enriched layer with oxygen and outer layer identified as a mixture oxides of Ni and Fe with uneven thickness between 3 and 10 μm. As shown in Figure 14, the corrosion product layer formed on IN 625 samples from thermal cycling experiment consists of a thinner inner corrosion oxide layer (4.5 μm in average) than that under isothermal condition. Cr-enrichment was found at the interface of alloy/oxide, together with an external Ni-rich layer which were considered as protective against further corrosion from molten salt.

Referring to In 825, the thickness of corrosion oxide layer formed from isothermal immersion experiment ranges from 9-14 μm, and consist of an outer iron oxide layer and inner mixed oxides of Cr and Ni. Referring to the EDX line scan (Figure 15 (a)) and literature (Kruizenga and Gill, 2014), sodium was present in the oxidation products in the form of $NaFeO_2$. This is a typical corrosion oxide layer at temperatures above 600°C (Bradshaw and Goods, 2001a). Sodium iron oxide provides little protection and is easily removed and/or spalled by slightly sanding the surface(Zhang et al., 2020). The non-uniformity of the corrosion layer thickness observed after isothermal corrosion test for In 825 in this study is caused by the loose iron oxide layer (Walczak et al., 2018). The spallation of iron oxide layer was found in Figure 15 (b), where iron oxide tended to spall due to its poor porosity and bad adherence to the bulk material. Fe depleted areas were found at the interface of oxide/alloy, where oxides of Ni and Cr were present as a protective layer from further metal interactions with molten salt. Thinner and more uniform corrosion layers were found without spallation on cross-section of samples from thermal cycling experiments when compared with samples from isothermal immersion test on In 825. In Figure 16, a double corrosion layer, with the thickness of around 6.5 μm is observed, and consisted of inner iron oxide and Ni oxide (Cr oxide).

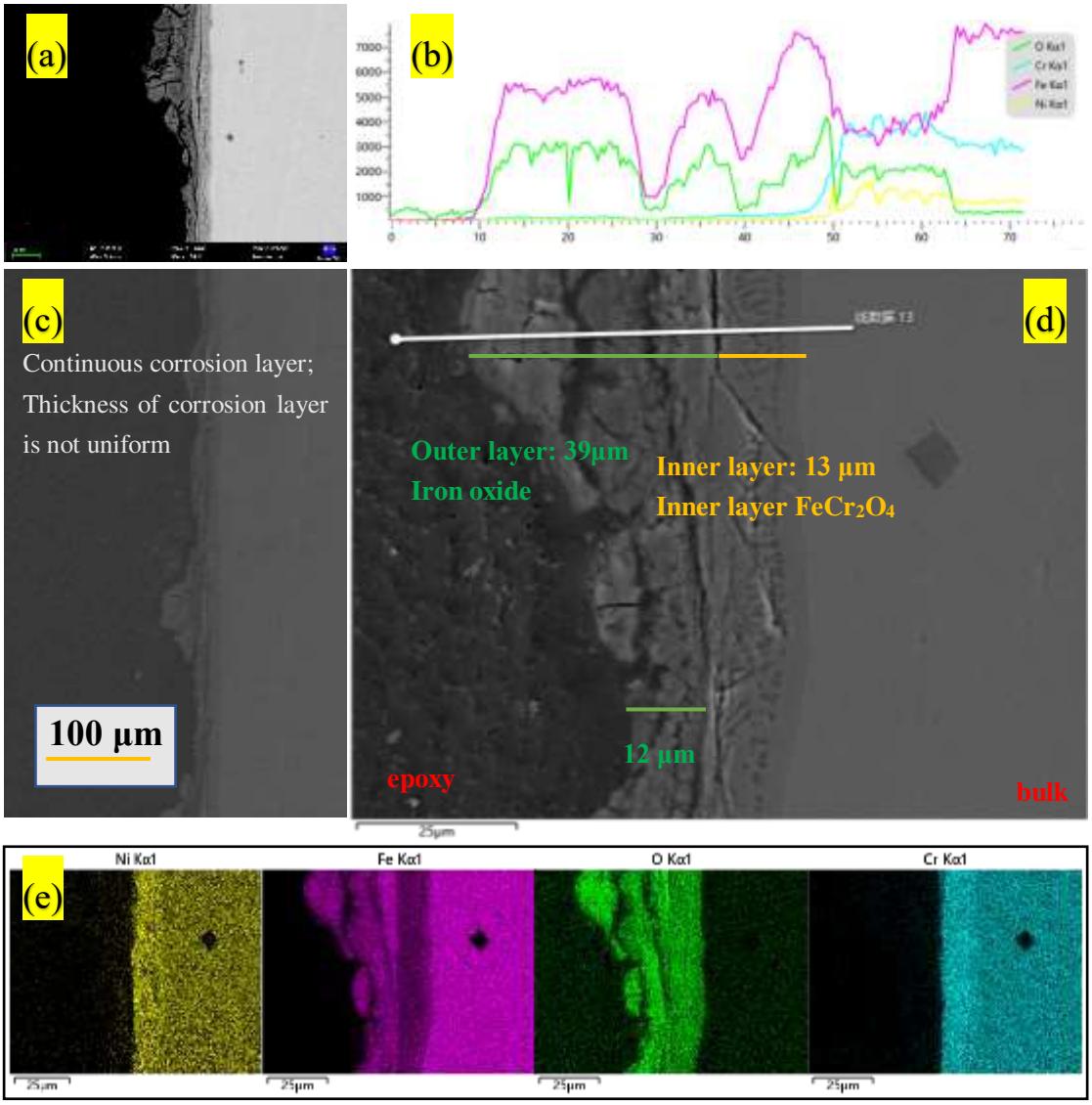

Figure 9: SEM-EDX profile of AISI 321 after 7-day isothermal immersion in solar salt at 600°C

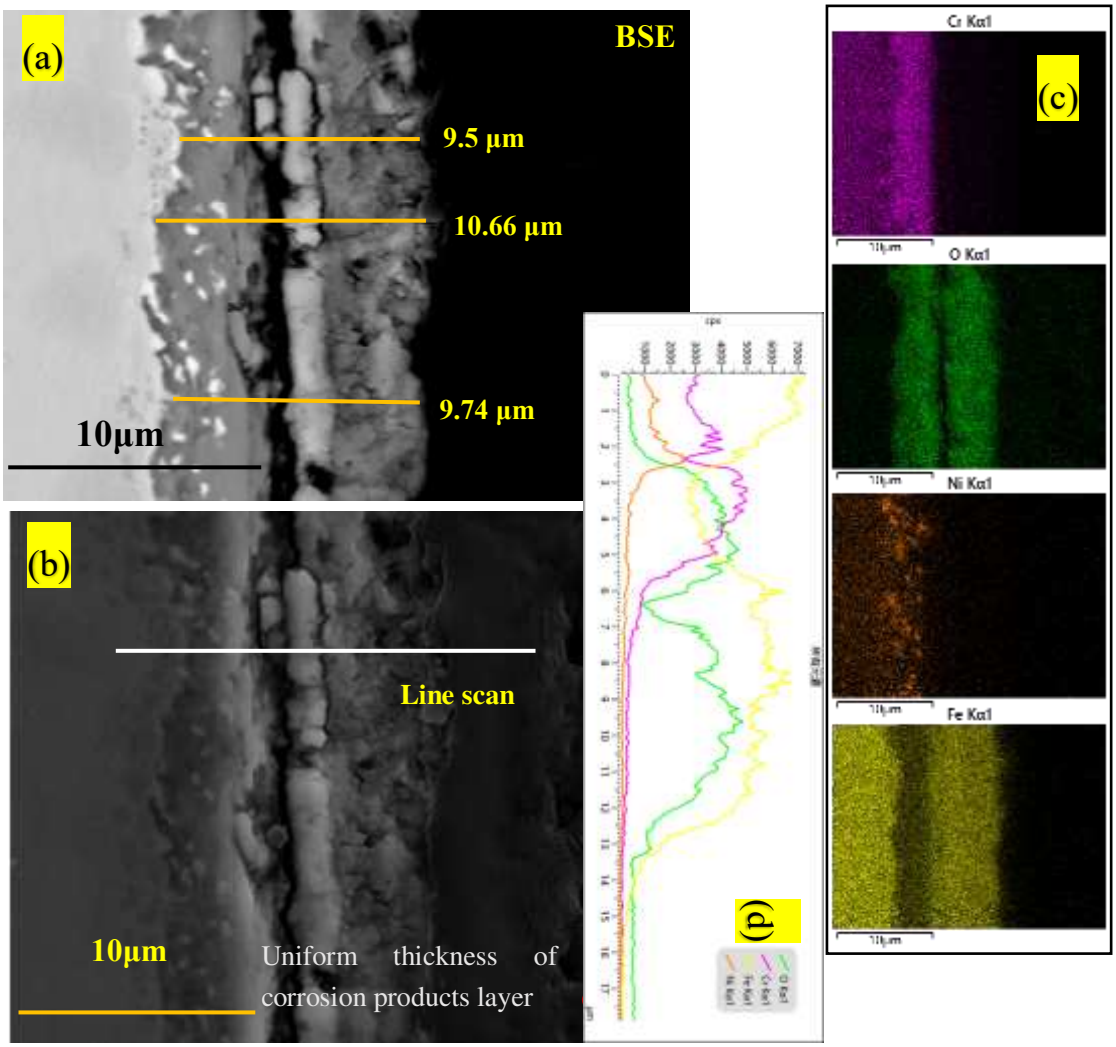

425

426 **Figure 10: SEM-EDX profile of AISI 321 after 7-day thermal cycling immersion in solar salt**

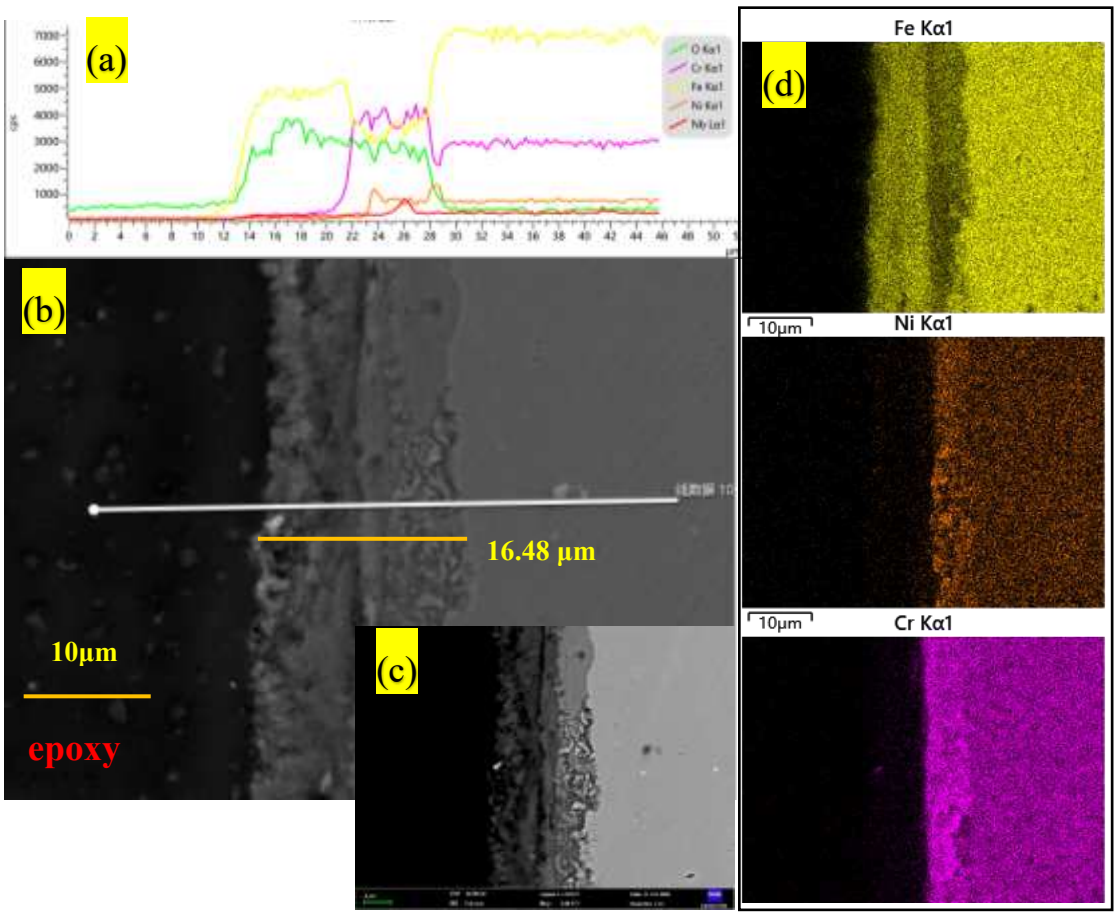

Figure 11: SEM-EDX profile of AISI 347 after 7-day isothermal immersion in solar salt at 600°C

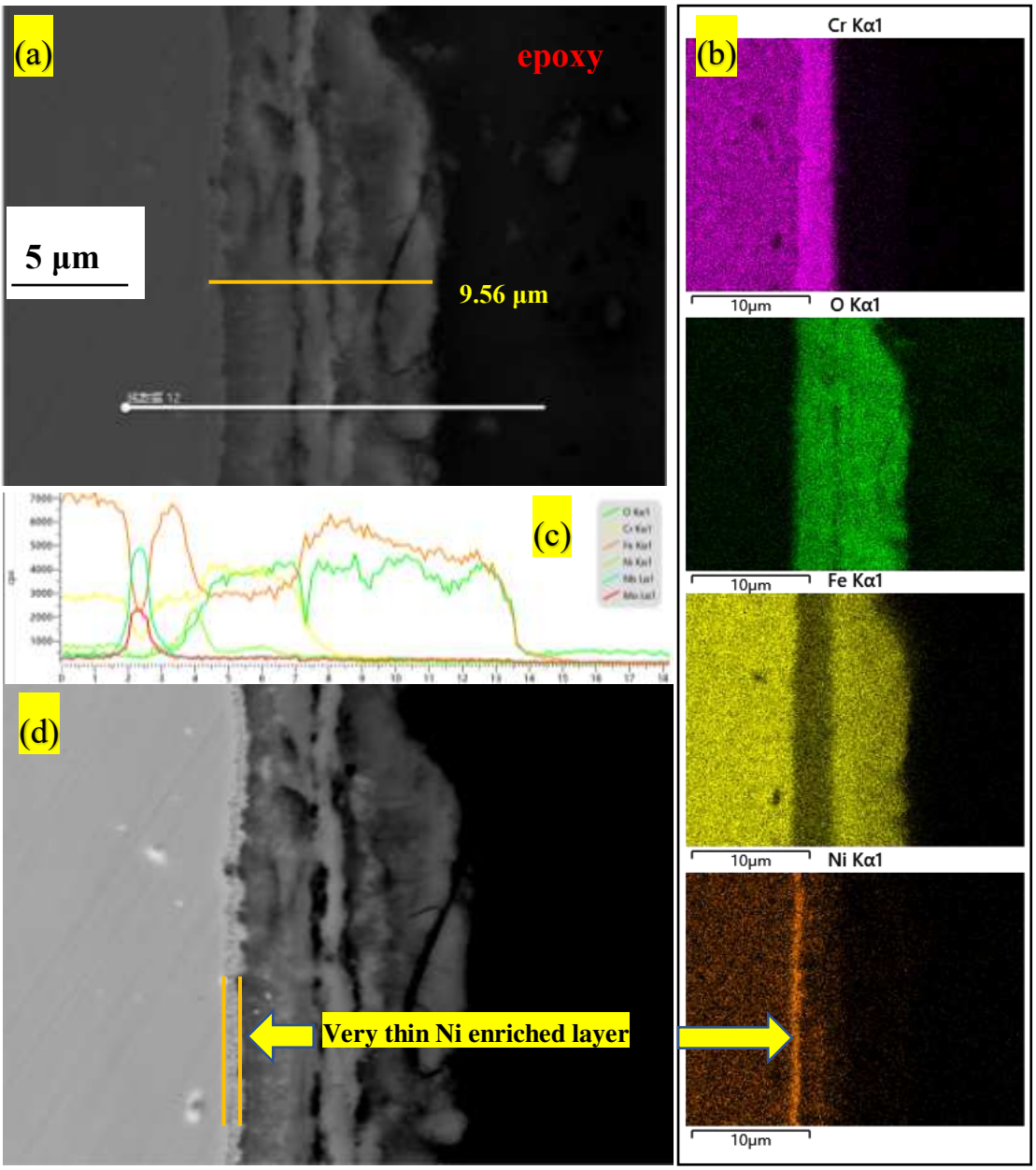

Figure 12: SEM-EDX profile of AISI 347 after 7-day thermal cycling immersion in solar salt

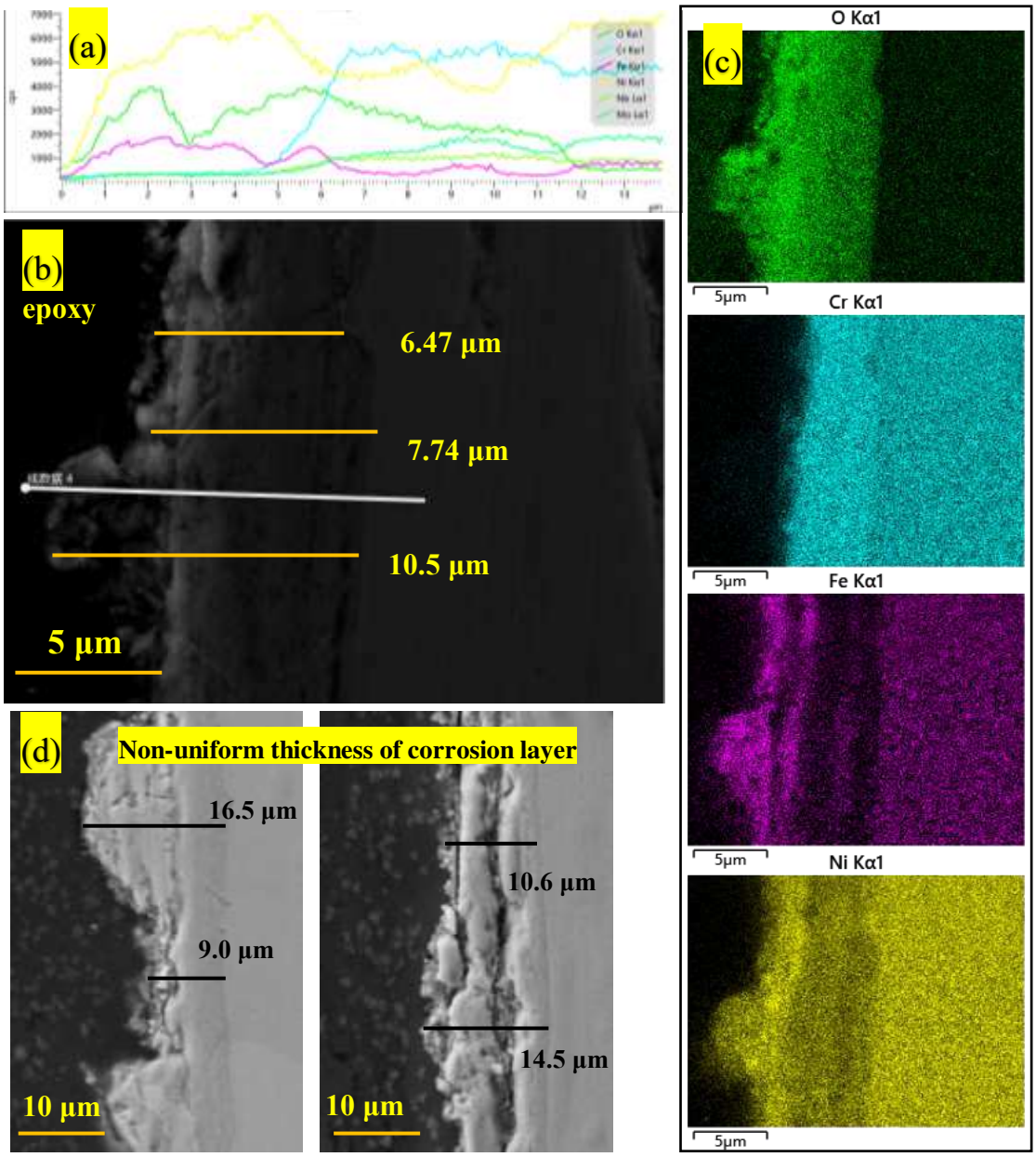

Figure 13: SEM-EDX profile of IN 625 after 7-day isothermal immersion in solar salt at 600°C

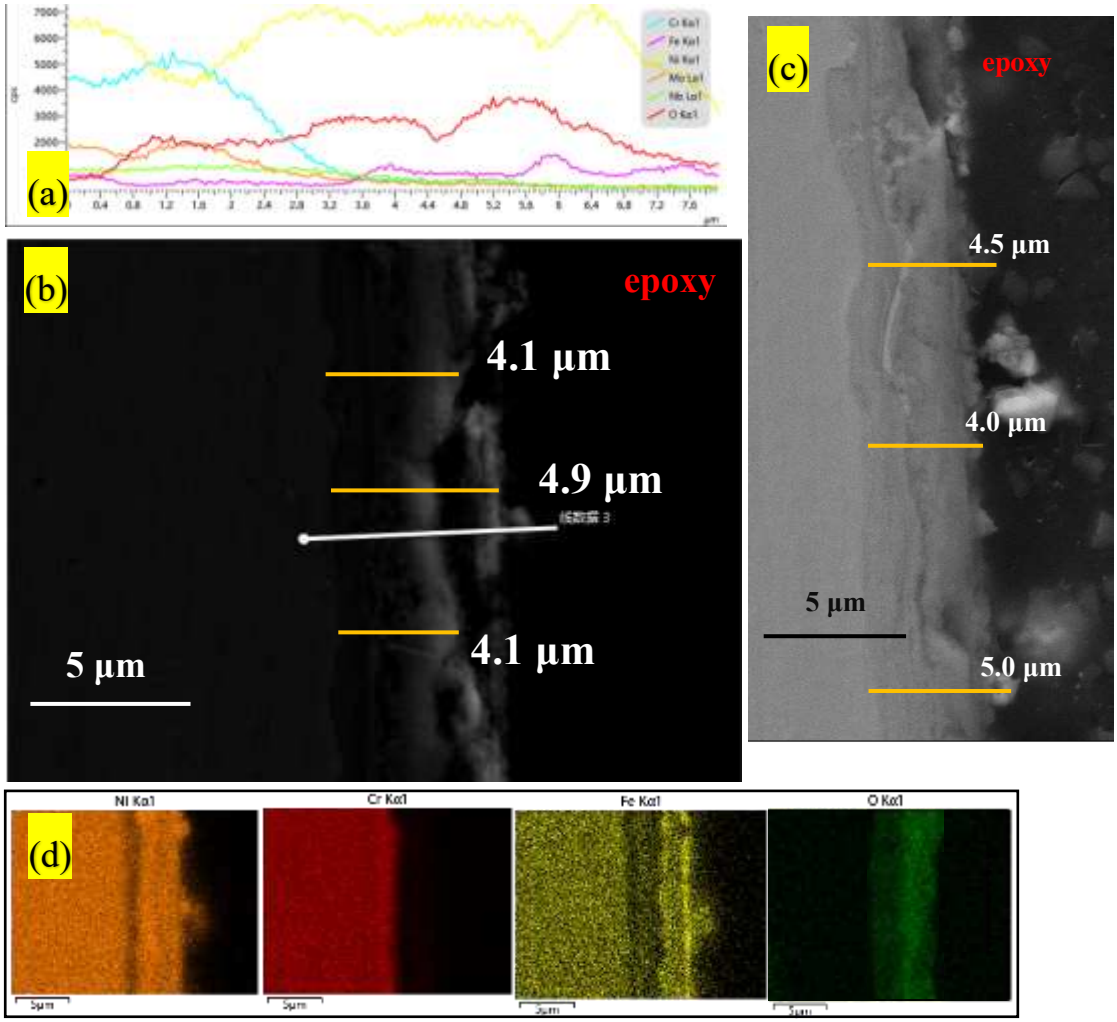

Figure 14: SEM-EDX profile of IN 625 after 7-day thermal cycling immersion in solar salt

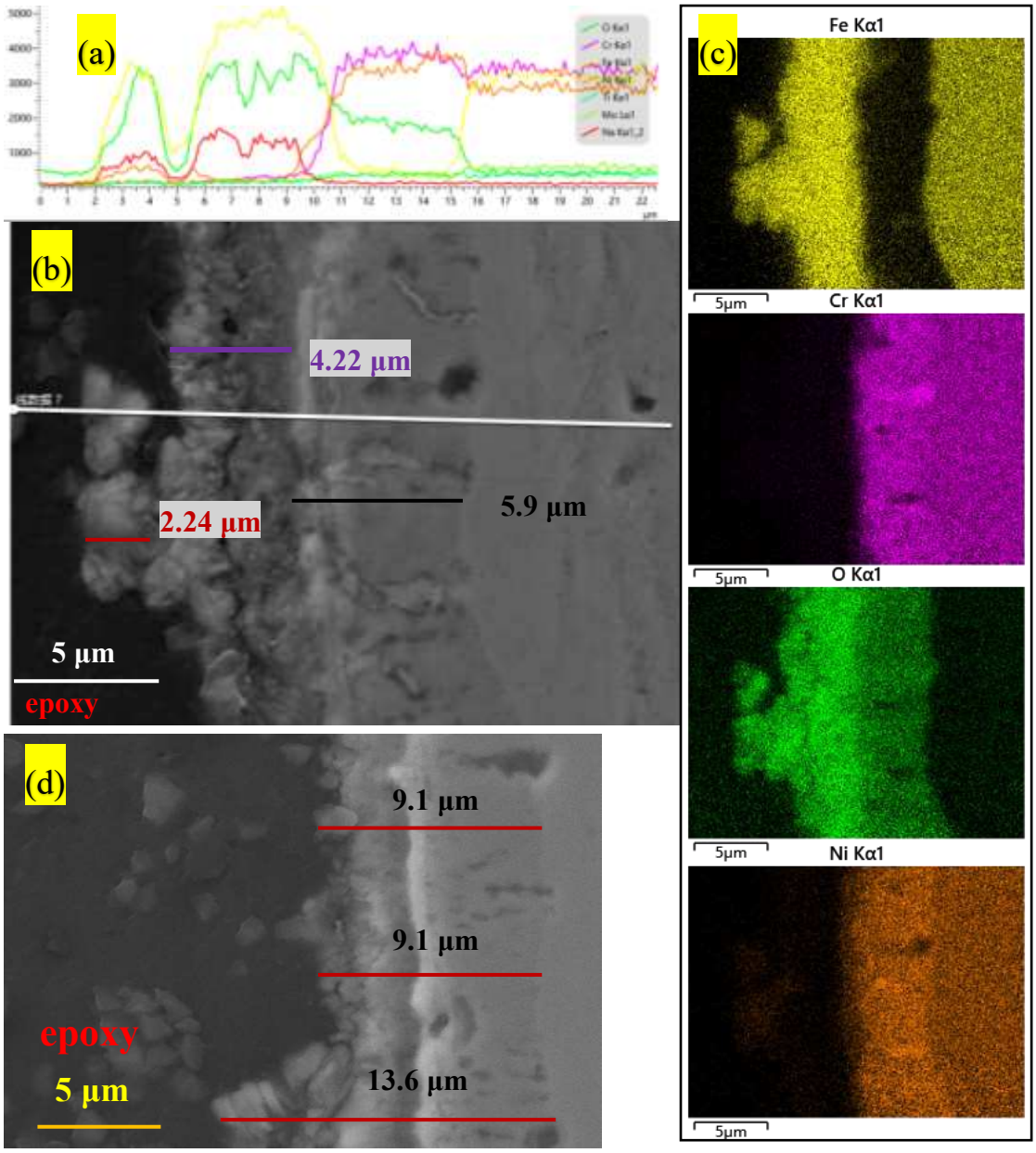

Figure 15: SEM-EDX profile of In 825 after 7-day isothermal immersion in solar salt at 600°C

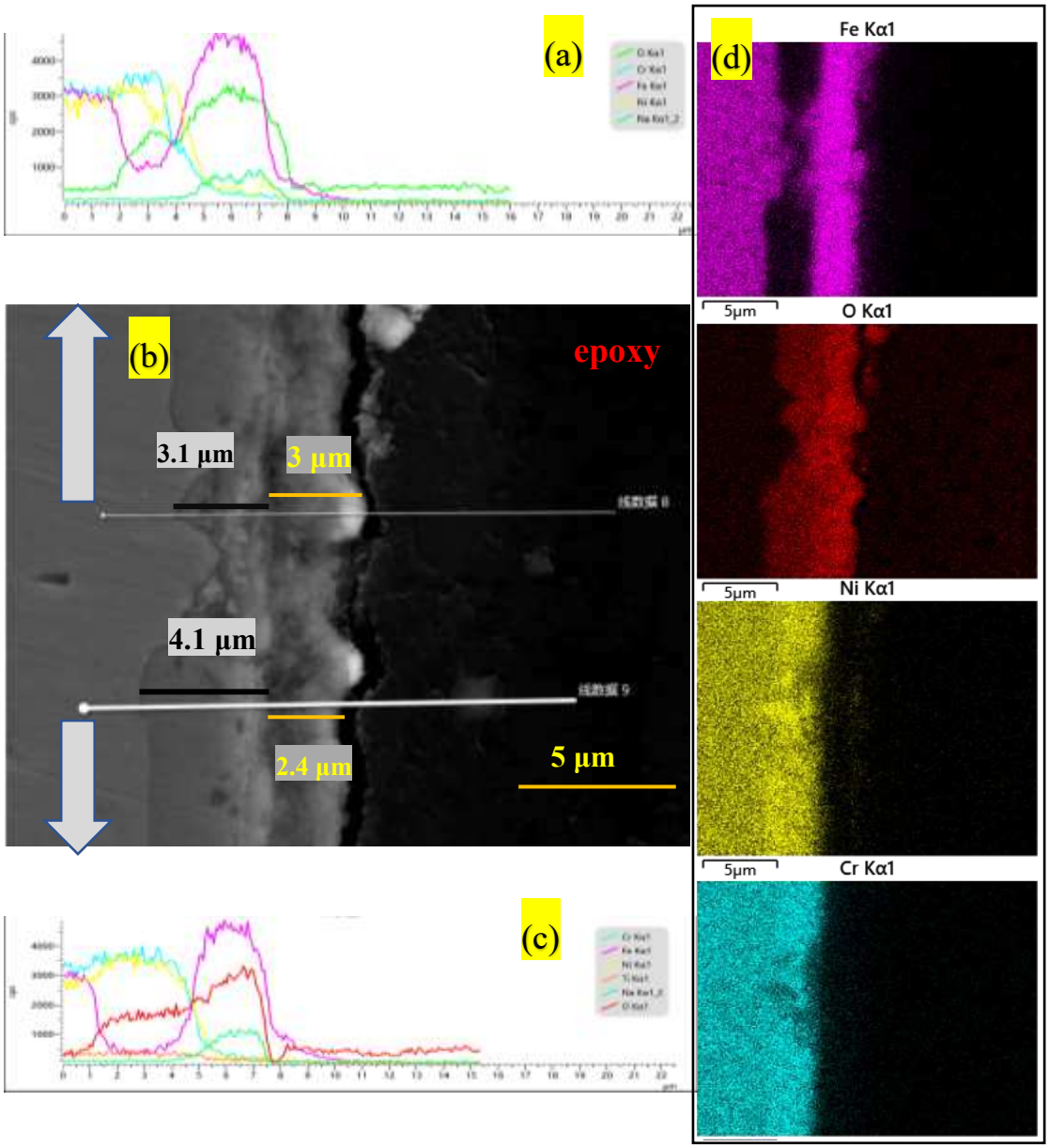

Figure 16: SEM-EDX profile of In 825 after 7-day thermal cycling immersion in solar salt

Discussion

The corrosion rate (CR) obtained from mass loss and depth of corrosion layer is summarised in Table 6 (the unit of CR was modified to µm/week). The CR of studied alloys obtained from mass loss and cross-sectional analysis show similar trends with the corrosion resistance of investigated alloys following this order: IN 625 > In 825 > AISI 347 > AISI 321. The CR from isothermal tests is 1.5-5 times higher than that under thermal cycling condition. This is different from the conclusion reported in the literature (Bradshaw and Goods, 2001b) on thermal cycling. However, the thermal cycling experiment protocol published by Sandia Laboratory (Bradshaw and Goods, 2001b) was based on a 7.5 h residence time at the maximum temperature of 565 °C and 0.5 hours cooling in ambient air at 95°C for 500 cycles. They (Bradshaw and Goods, 2001b)

reported that thermal cycling increased the corrosion rate of the three stainless steels moderately when compared to isothermal immersion corrosion tests. The difference in the results obtained and conclusions from this study is likely due the longer residence time for the cooling process; 12 hrs between peak and lowest temperatures per cycle, and corresponding effect of extended duration at lower temperatures in the cycle.

Due to the continuous immersion in molten salt at 600˚C during isothermal tests, the oxide layers on formed have more potential to breakdown and spall off (Encinas-Sánchez et al., 2019). In comparison, the intermittent cooling process or period of immersion at lower temperature during thermal cycling interrupts the continuous thermal effects on the formation and stability of oxide layers, thus reducing the potential for breakdown and spallation of the oxide layers. The spallation behaviour is linked to the instability of oxide layers at high temperatures. The thermal expansion and contraction of corrosion layers is expected to occur during thermal cycling due to the regular change of temperature. Despite the difference in coefficients of thermal expansion and elastic modules of base metal between corrosion layers (Yin et al., 2021), the cooling effect during thermal cycling for 12 hours per 24 hour cycle, induces lower thermal stresses to help to improve the adherence of corrosion multi-layers than in cooling-free isothermal process (Bradshaw and Goods, 2001b). It's worth noting that any residual thermal stress (Yin et al., 2021) caused by cooling process during thermal cycling between multi-layers in this study is likely to be significantly lower than thermal stress levels expected from simulated thermal shock experiments (Bradshaw and Goods, 2001b). The evidence from this studies clearly shows that thermal cycling relieves and delays the thermal effect on the multi-layers, and the tendency for spallation to occur.

Solar salt is known to remain stable at temperatures up to 565 ˚C and will decompose into nitrite salt and oxide ions (Walczak et al., 2018) at higher temperature, thus increasing the corrosivity of the molten salt and the corrosion rate of exposed alloys (Bell et al., 2019). Longer residence at 600 ˚C for isothermal test means that more oxide ions are available within in a progressively increasing corrosive molten salt system than in thermal cycling test (Bonk et al., 2020). The effect of thermal cycling therefore reduces the corrosiveness of the system by slowing down the decomposition process.

Furthermore, referring to the Figure 9-Figure 16, a double oxide layer was observed at the corrosion interface. An Inner Cr-rich oxides film acts as protective layer against corrosion because of low diffusion rate of oxygen and metal ions through the film (Gui et al., 2017) and outer Fe-rich layer protect the dissolution of the inner Cr-rich oxide into salt. The diffusion order of metal ions in Cr-oxides is $D_{Fe}>D_{Ni}>D_{Cr}$ (Lobnig et al., 1992). Atomic diffusion is enhanced by increasing temperature and duration of tests (Bataillou et al., 2018). Longer residence time of immersion at 600˚C for isothermal test is believed to promote the outward diffusion of Fe and Cr from the base material, resulting in forming thicker corrosion layers than in samples from thermal cycling tests. The mechanisms by which thermal cycling is likely to influence the rate of material degradation and corrosion layer behaviours in the long term still needs to be investigated.

Table 6: Corrosion rate obtained from mass loss and depth of corrosion (uniform unit: µm/week, ISO and TC indicates isothermal and thermal cycling)

Material/ condition	Inner layer µm	Outer layer µm	Total thickness µm/w	Corrosion rate from mass loss	
				µm/year	µm/w
AISI 321 ISO	13	12-39	25-52	434	8.32
AISI 321 TC	4.2	5.8	10	114	2.2
AISI 347 ISO	8	8.4	16.4	317	6.08
AISI 347 TC	4.25	5.3	9.56	124	2.38
IN 625 ISO	6.47	3-10	9.5-16.5	128	2.45
IN 625 TC	1.8	2.7	4.5	57.7	1.11
In 825 ISO	5.9	3.2-7.7	9.1-13.6	109	2.09
In 825 TC	3.6	2.7	6.3	80.8	1.55

The corrosion layer of Ni-based alloy is thinner than that of stainless steels, indicating that AISI 321 and AISI 347 experienced a more severe corrosion process than IN 625 and In 825 from cross-section observation. The double corrosion layer was formed on the surface of stainless steel, and the main corrosion product is an outer sodium iron oxide/iron oxide and inner iron chromium oxide. The occurrence of non-uniformity in corrosion thickness for stainless steels is caused by the spallation of the poorly adhered corrosion layer, which often occurs in isothermal immersion tests. The corrosion products formed on the stainless-steel surface have been previously reported and are also confirmed in this study to be Fe_2O_3 and Fe_3O_4 (Zhang et al., 2020) based on the following **Equation 3** to **Equation 7** (Hu et al., 2018).

$$\boldsymbol{NO_3^- + 2e^- \leftrightarrow NO_2^- + O^{2-}} \qquad \textbf{Equation 3}$$

$$\boldsymbol{Fe + O^{2-} \rightarrow FeO + 2e^-} \qquad \textbf{Equation 4}$$

$$\boldsymbol{FeO + O^{2-} \rightarrow Fe_3O_4 + 2e^-} \qquad \textbf{Equation 5}$$

$$\boldsymbol{Fe_3O_4 + O^{2-} \rightarrow Fe_2O_3 + 2e^-} \qquad \textbf{Equation 6}$$

$$\boldsymbol{\frac{1}{2}Fe_2O_3 + \frac{1}{2}O^{2-} + Na^+ \rightarrow NaFeO_2} \qquad \textbf{Equation 7}$$

Sodium and potassium nitrate always exhibited weak basic melt below 570°C and iron forms a passive oxide layer to mitigate the diffusion of soluble chromium from the metal substrate (Bell et al., 2019). Above the temperature of 570°C and close to 600°C, the basicity increases significantly as the decomposition reaction in **Equation 3** from nitrate to nitrite becomes more favourable (Bell et al., 2019; Bradshaw and Goods, 2001a). Meanwhile, according to **Equation 7** the iron outer layer is converted to sodium ferrite ($NaFeO_2$) which is non-protective and consequently results in the corrosion rate increasing (Bradshaw and Goods, 2001a). In this study, the $NaFeO_2$ was identified as the corrosion product on the surface of stainless steels samples from SEM–EDX analysis and XRD patterns in Figure 7 and Figure 8, respectively. This is also

observed in terms of the distribution of elements from cross-sectional analysis of the alloy–oxide layer interface. The Cr and Ni enriched region was observed in the inner oxide layer line scan due to the selective dissolution and diffusion disparity of alloy elements. Zhang et.al. (Zhang et al., 2020) reported that the corrosion products of (Fe, Cr, Ni)$_3$O$_4$ mixed oxide spinel are probably present in the inner oxide layer and widely proven to improve the stainless steel corrosion resistance (Hua et al., 2019; Liu et al., 2017; Soleimani Dorcheh and Galetz, 2016) by **Equation 8 - Equation 11**. In this study, $FeCr_2O_4$ is the main oxide spinel and well adhered to the bulk material.

$$\boldsymbol{Ni + O^{2-} \rightarrow NiO + 2e^-} \qquad \textbf{Equation 8}$$

$$\boldsymbol{Cr + 3/2O^{2-} \rightarrow 1/2Cr_2O_3 + 3e^-} \qquad \textbf{Equation 9}$$

$$\boldsymbol{FeO + Cr_2O_3 \rightarrow FeCr_2O_4} \qquad \textbf{Equation 10}$$

$$\boldsymbol{NiO + Cr_2O_3 \rightarrow NiCr_2O_4} \qquad \textbf{Equation 11}$$

For nickel-based alloys, they exhibited better corrosion resistance than stainless steels in this study as shown by the result from mass loss measurements and SEM observation. Several researchers have reported that Ni-based alloys corrosion is insignificant at temperatures below 550°C (Kruizenga et al., 2013) with it proving difficult to obtain any corrosion information through typical SEM/XRD methods (Walczak et al., 2018) at 500°C. According the results above, Ni oxide and iron chromium oxide are the main corrosion product formed on the surface of Ni-based alloys, formed through **Equation 8**, **Equation 9** and **Equation 10**. IN 625 shows mixed Fe and Ni oxides at the outer layer and Cr oxide at the inner layer, while outer Fe oxide layer and inner (Ni, Cr) oxides form part of the corrosion product layer of In 825 in both isothermal or thermal cycling experiments.

In this study, the oxygen consumed for the formation of interfacial oxide layers is linked to the decomposition of nitrate ion to nitrite, especially at temperature of 600°C since test were performed in argon.

Conclusion

The corrosion behaviour of stainless steels; AISI 321 and AISI 347, and Ni-based alloys; IN 625 and In 825 in solar salts used in concentrated solar power plants were experimentally investigated under isothermal (at 600°C) and thermal cycling conditions (temperatures between 250-600°C) under argon atmosphere. The results of corrosion performance were comparatively studied to evaluate and understand the corrosion mechanism. The main conclusions are as follows.

1. The interaction of stainless steels and nickel alloys with molten salts led to the formation of multi-layered interfacial oxides in both isothermal and thermal cycling conditions. They consist mainly of an inner layer of Fe_2O_3/Fe_3O_4/ $FeCr_2O_4$ and an outer layer of $NaFeO_2$ on stainless steels: AISI 321 and AISI 347, and an inner layer of NiO and/or $FeCr_2O_4$ on Ni-based alloy: IN 625 and In 825. Also an outer layer of $NaFeO_2$ was found on the surface of In 825.

2. The main driving force for material loss is linked to the rate of spallation loosely held, porous, and poorly adherent Sodium–Iron spinel ($NaFeO_2$) layer. This layer easily spalls off to expose the inner and more protective $FeCr_2O_4$ and Fe_3O_4 layer (for stainless

steels), and NiO and/or $FeCr_2O_4$ (for Nickel alloys) to further degradation by molten salt species. This process is more dominant under isothermal conditions and mitigated by the thermal cycles used in this study.

3. Rate of material loss was higher in samples from isotheral immersion test at 600 °C than in samples from thermal cycling immersion tests between 250 and 600°C. This was observed for both stainless steel samples and samples from Nickel alloys, and believed to be linked to the effect of intermittent night – time cooling over a 12 h residence time at 250°C on the stability and adherence of interfacial oxide layers.

4. The increase in corrosion rate under isothermal conditions is due to increase in the rate of decomposition of nitrate salts to nitrite. This increases the aggressiveness of the corrosion media. This effect is suppressed under thermal cycling conditions.

5. The combined effect of 12 h residence time at 250°C and short experiment duration helped to understand the potential synergy of thermal fatigue effect from thermal cycling and electrochemical activities of molten salt species on the rate of spallation of interfacial oxide layers and overall material loss rate.

Declaration of competing interest

The authors declared that they have no conflicts of interest to this conflict of interest to this manuscript.

Acknowledgements

Special thanks to Dr Stuart Micklethwaith in LEMAS for his help on SEM surface observation. The authors acknowledge the funding and support from Zhejiang JIULI Hi-tech Metals Co., Ltd through the Jiuli Hi-tech Metals Co – University of Leeds corrosion integrated centre.

Data Availability

The raw/processed data required to reproduce these findings cannot be shared at this time as the data also forms part of an ongoing study.

CRediT authorship contribution statement

Qingyang Liu: Conceptualization, Methodology, Formal analysis, Investigation, Resources, Writing - original draft. **Richard Barker**: Supervision, Writing - review & editing. **Chun Wang**: Supervision, Writing - review & editing. **Jiong Qian**: Review & editing. **Anne Neville**: Resources, Review & editing, Supervision. **Frederick Pessu**: Supervision, Methodology, Writing - review & editing, Resources, Conceptualization.

References

Alva, G., Lin, Y., Fang, G., 2018. An overview of thermal energy storage systems. Energy 144, 341-378.

Bataillou, L., Desgranges, C., Martinelli, L., Monceau, D., 2018. Modelling of the effect of grain boundary diffusion on the oxidation of Ni-Cr alloys at high temperature. Corrosion Science 136, 148-160.

Bell, S., Steinberg, T., Will, G., 2019. Corrosion mechanisms in molten salt thermal energy storage for concentrating solar power. Renewable and Sustainable Energy Reviews 114.

Bonk, A., Braun, M., Sötz, V.A., Bauer, T., 2020. Solar Salt – Pushing an old material for energy storage to a new limit. Applied Energy 262, 114535.

Bradshaw, R.W., Goods, S.H., 2001a. Corrosion of alloys and metals by molten nitrates. Sandia National Lab.(SNL-CA), Livermore, CA (United States).

Bradshaw, R.W., Goods, S.H., 2001b. Corrosion resistance of stainless steels during thermal cycling in alkali nitrate molten salts. Sandia National Laboratories.

Desideri, U., Campana, P.E., 2014. Analysis and comparison between a concentrating solar and a photovoltaic power plant. Applied Energy 113, 422-433.

Encinas-Sánchez, V., de Miguel, M.T., Lasanta, M.I., García-Martín, G., Pérez, F.J., 2019. Electrochemical impedance spectroscopy (EIS): An efficient technique for monitoring corrosion processes in molten salt environments in CSP applications. Solar Energy Materials and Solar Cells 191, 157-163.

Encinas-Sánchez, V., Lasanta, M.I., de Miguel, M.T., García-Martín, G., Pérez, F.J., 2020. Corrosion monitoring of 321H in contact with a quaternary molten salt for parabolic trough CSP plants. Corrosion Science, 109070.

G1-03, A., 2017. Standard Practice for Preparing, Cleaning, and Evaluating Corrosion Test Specimens. www.astm.org.

Gates-Rector, S., Blanton, T., 2019. The Powder Diffraction File: a quality materials characterization database. Powder Diffraction 34(4), 352-360.

Gomes, A., Navas, M., Uranga, N., Paiva, T., Figueira, I., Diamantino, T.C., 2019. High-temperature corrosion performance of austenitic stainless steels type AISI 316L and AISI 321H, in molten Solar Salt. Solar Energy 177, 408-419.

Goods, S.H., Bradshaw, R.W., 2004. Corrosion of Stainless Steels and Carbon Steel by Molten Mixtures of Commercial Nitrate Salts. Journal of Materials Engineering and Performance 13(1), 78-87.

Gui, Y., Meng, X.B., Zheng, Z.J., Gao, Y., 2017. Critical temperature determination of detectable Cr diffusion enhancement by nanostructure through structural evolution analysis of the oxide films at 25–450°C on 304 stainless steel. Applied Surface Science 419, 512-521.

Han, Y., Zhang, C., Wu, Y., Lu, Y., 2021. Investigation on thermal performance of quaternary nitrate-nitrite mixed salt and solar salt under thermal shock condition. Renewable Energy 175, 1041-1051.

Hu, Y., Han, Y., Qin, Y., Zhou, H., 2018. Corrosion Behavior of 45 Steel in Molten Nitrate Salts with 3wt% Impurities at 773.15K. IOP Conference Series: Materials Science and Engineering 394, 032117.

Hua, Y., Xu, S., Wang, Y., Taleb, W., Sun, J., Zhang, L., Barker, R., Neville, A., 2019. The

formation of FeCO3 and Fe3O4 on carbon steel and their protective capabilities against CO2 corrosion at elevated temperature and pressure. Corrosion Science 157, 392-405.

Kruizenga, A., Gill, D., 2014. Corrosion of Iron Stainless Steels in Molten Nitrate Salt. Energy Procedia 49, 878-887.

Kruizenga, A.M., Gill, D.D., LaFord, M., McConohy, G.J.A.S.N.L.S.-. 2013. Corrosion of High Temperature Alloys in Solar Salt at 400, 500, and 680 C.

Liu, B., Wei, X., Wang, W., Lu, J., Ding, J., 2017. Corrosion behavior of Ni-based alloys in molten NaCl-CaCl 2 -MgCl 2 eutectic salt for concentrating solar power. Solar Energy Materials and Solar Cells 170, 77-86.

Lobnig, R., Schmidt, H., Hennesen, K., Grabke, H.J.O.o.M., 1992. Diffusion of cations in chromia layers grown on iron-base alloys. 37(1), 81-93.

Pelay, U., Luo, L., Fan, Y., Stitou, D., Rood, M., 2017. Thermal energy storage systems for concentrated solar power plants. Renewable and Sustainable Energy Reviews 79, 82-100.

Soleimani Dorcheh, A., Durham, R.N., Galetz, M.C., 2016. Corrosion behavior of stainless and low-chromium steels and IN625 in molten nitrate salts at 600 °C. Solar Energy Materials and Solar Cells 144, 109-116.

Soleimani Dorcheh, A., Galetz, M.C., 2016. Slurry aluminizing: A solution for molten nitrate salt corrosion in concentrated solar power plants. Solar Energy Materials and Solar Cells 146, 8-15.

Stott, F., Wei, F., 1989. High temperature oxidation of commercial austenitic stainless steels. Materials science and technology 5(11), 1140-1147.

Trent, M., Goods, S., Bradshaw, R., 2016. Comparison of corrosion performance of grade 316 and grade 347H stainless steels in molten nitrate salt, AIP Conference Proceedings. AIP Publishing LLC, p. 160017.

Walczak, M., Pineda, F., Fernández, Á.G., Mata-Torres, C., Escobar, R.A., 2018. Materials corrosion for thermal energy storage systems in concentrated solar power plants. Renewable and Sustainable Energy Reviews 86, 22-44.

Yin, Y., Tan, Q., Zhao, Y., Sun, Q., Shi, Z., Bermingham, M., Zhuang, W., Huang, H., Zhang, M.-X., 2021. A cost-effective Fe-rich compositionally complicated alloy with superior high-temperature oxidation resistance. Corrosion Science 180, 109190.

Zhang, X., Zhang, C., Wu, Y., Lu, Y., 2020. Experimental research of high temperature dynamic corrosion characteristic of stainless steels in nitrate eutectic molten salt. Solar Energy 209, 618-627.